AALTO UNIVERSITY
School of Engineering
Department of Applied Mechanics

Torsten Malm

Simulation of Wind Fields at Scharffenbergbotnen, Antarctica and their Impact on Blue Ice Areas

Master's Thesis submitted in partial fulfillment of the requirements for the degree of Master of Science in Technology.

October 14, 2011

Supervisor: Professor Jukka Tuhkuri

Instructor: Thomas Zwinger, Dr.

Aalto University
School of Engineering

AALTO UNIVERSITY
School of Engineering

ABSTRACT OF THE
MASTER'S THESIS

Author:	Torsten Malm		
Name of the Thesis:	Simulation of Wind Fields at Scharffenbergbotnen, Antarctica and their Impact on Blue Ice Areas		
Date:	October 14, 2011	**Number of pages:**	69
Language:	English		
Department:	Department of Applied Mechanics		
Professorship:	Kul-49 Mechanics of Materials		
Supervisor:	Professor Jukka Tuhkuri		
Instructor:	Thomas Zwinger, Dr.		

The focus of this thesis is on numerical simulation of local wind fields governed by the incompressible and time-dependent Navier-Stokes equations. A Large Scale Computational Fluid Dynamics Finite Element code ELMER is used to resolve the local wind fields in Scharffenbergbotnen, Antarctica, and thus provide information of possible snow re-distribution patterns. It is assumed that the winds play a big role in the formation of Blue Ice Areas, which at Scharffenbergbotnen have been utilized as a proxy for reconstruction of paleoclimatological data.

The main objective is to resolve the wind field patterns and not the actual distribution of the snow. This is done by using a Variational Multiscale Method with the Finite Element Method. This method is considered to be a powerful tool for solving high Reynolds-number turbulent flows. The goal of this thesis is to get an understanding on whether the local winds combined with the katabatic winds that occur in these areas can achieve the strengths to clear the blue ice areas of the usually forming densifying snow layer that accumulates on the ice.

Our results clearly indicate that the magnitude of the absolute velocity and shear stress increase at the blue ice areas. However, due to the lack of data and by assumptions of the applied methods, this is rather a proof of concept, and the results have to be interpreted qualitatively rather than quantitatively.

Keywords: Turbulence, Variational Multiscale Method, Scharffenbergbotnen, Antarctica, Blue Ice Areas, The Finite Element Method, Katabatic Winds, ELMER

Aalto-yliopisto
Insinööritieteiden
korkeakoulu

AALTO-YLIOPISTO DIPLOMITYÖN
Insinööritieteiden Korkeakoulu TIIVISTELMÄ

Tekijä:	Torsten Malm
Työn nimi:	Ilmavirtausten mallintaminen Scharffenbergbotnenissa, Antarktiksella ja niiden vaikutus sinisiin jää alueisiin
Päivämäärä:	14. lokakuuta 2011 **Sivuja:** 69
Kieli:	Englanti
Laitos:	Sovelletun mekaniikan laitos
Professuuri:	Kul-49 Lujuusoppi
Työn valvoja:	Professori Jukka Tuhkuri
Työn ohjaaja:	Tohtori Thomas Zwinger

Tässä diplomityössä tarkoituksena on tehdä numeerista mallinnusta paikallisista tuulista Scharffenbergbotnenissa, Antarktiksella. Mallintamiseen käytetään kokoonpuristumattomia ja ajasta-riippuvaisia Navier-Stokes yhtälöitä. Elementtimenetelmä ohjelmaa ELMER:iä käytetään paikallisten ilmavirtojen mallintamiseen, jotta voitaisiin saada käsitys tuulien vaikutuksesta lumen siirtymiseen sinisillä jäillä. Scharffenbergbotnenin siniset jäät ovat olleet tärkeä paleoklimatoloogisen tiedon lähde. Tutkimuksen pääasiallinen tarkoitus on kuitenkin ilmavirtausten laskeminen eikä lumen jakautumisen mallintaminen.

Ilmavirtojen ratkaisemiseen käytetään niin sanottua Variational Multiscale menetelmää elementtimenetelmän yhteydessä. Menetelmää pidetään erittäin tehokkaana välineenä turbulenssin ratkaisemiseen. Tavoitteena on saada tietoa siitä, voivatko paikalliset tuulet yhdessä alueella vallitsevien katabaattisten ilmavirtojen kanssa olla paikallisesti niin voimakkaita, että ne ”puhdistaisivat” kyseiset sinisen jään alueet lumesta.

Tulokset viittaavat siihen, että absoluuttinen tuulen nopeus sekä leikkausjännitykset sinisten jäiden alueilla ovat selvästi muita alueita voimakkaammat. Käytetty malli on tosin hyvin yksinkertaistettu ja simuloimiseen käytetty data oli erittäin rajallinen. Näin ollen tutkimustuloksia voidaan lähinnä pitää suuntaa antavina ja aikaisempia käsityksiä vahvistavina. Tutkimusta voidaan siis pitää kvalitatiivisena.

Avainsanat: Turbulenssi, Variational Multiscale Method, Scharffenbergbotnen, Antarktis, Siniset Jäät, Elementti Menetelmä, Katabaattiset Tuulet, ELMER

Acknowledgements

This Master's thesis has been of major interest for me, and I have learned numerous things during the process. When I started this project I had very little knowledge of turbulence modeling and working on this thesis I came to understand that the world of turbulence and turbulence modeling is not at all straight forward, and much more chaotic than one would ever imagine. Fortunately I have had the opportunity to work with people that have a great understanding of the topic.

I especially want to thank my instructor Dr. Thomas Zwinger (CSC — IT Center for Science, Finland Ltd.) who has dedicated numerous hours of his time to work with me on this project. He has been a mentor and an insightful source of knowledge and he has given me the ability to look at problems from totally new perspectives. I would like to thank John Moore, Professor of Global Change and Earth System Science (University of Lapland and Beijing Normal University), who made this project possible.

I also want to express my gratitude to Professor Rolf Stenberg (Aalto University), Docent Mikko Lyly (ABB, Finland) and Dr. Peter Råback, (CSC — IT Center for Science, Finland Ltd.) who have never hesitated to help me with any questions what so ever. Thanks go to Dr. Annsa Sinisalo (University of Oslo), Dr. Martina Schäfer (University of Lapland), Sami Saarinen (CSC — IT Center for Science, Finland) and Professor Michiel van den Broeke (Utrecht University) for helping me retrieve the data needed for the simulations and Niklas Kullberg, M.Sc. (Aalto University) for the valuable help he has given me with post processing.

Last but not least, I would like to thank all of my family and friends who have supported me throughout this process.

Otaniemi, October 14, 2011

Torsten Malm

Contents

Abbreviations

ABL	Atmospheric Boundary Layer
BIA	Blue Ice Area
CFD	Computational Fluid Dynamics
DEM	Digital Elevation Model
DNS	Direct Numerical Simulation
ECMWF	European Centre for Medium Range Weather Forecasts
FE	Finite Element
FEM	Finite Element Method
lat	latitude
long	longitude
LES	Large Eddy Simulation
LSCFD	Large Scale Computational Fluid Dynamics
NSE	Navier-Stokes Equations
PDE	Partial Differential Equation
RANS	Reynolds Averaged Navier-Stokes equations
SBB	Scharffenbergbotnen
SD	Standard Deviation
UTM	Universal Transverse Mercator
VMS	Variational Multiscale

Nomenclature

ρ	density
τ	shear stress
$\bar{\bar{\varepsilon}}$	rate of strain tensor
u_n	normal component of velocity
$\vec{u}$	velocity vector
$\vec{n}$	normal vector
t	time
V	control volume
∂V	boundary of control volume
∇	gradient operator
$\nabla\cdot$	divergence operator
h	height above ground
x	spacial coordinate
y	spacial coordinate
z	spacial coordinate
X	material coordinate
Y	material coordinate
Z	material coordinate
m	mass

$\bar{\bar{\sigma}}$	the Cauchy stress tensor
p	pressure
$\bar{\bar{I}}$	identity matrix
$\bar{\bar{\mathbb{T}}}$	deviatoric stress
μ	viscosity
σ_{ii}	normal stress component
σ_{ij}	shear stress component
$\vec{F}$	force
$\vec{t}$	surface force, traction field
$\vec{f}$	body force
$\otimes$	outer product
ε_{ijk}	Levi-Civita symbol
δ_{ij}	Kronecker delta
$\vec{u}_0$	initial velocity vector
p_0	initial pressure
t_0	time at beginning
Ω	domain
$\partial\Omega$	boundary of domain
Γ_E	east boundary
Γ_N	north boundary
Γ_S	south boundary
Γ_W	west boundary
Γ_{top}	top boundary
Γ_{bed}	bed boundary

$\mathcal{V}^v$	solution function space for velocity
$\mathcal{V}^0$	solution function space for velocity, with $\vec{v} = \vec{0}$ on the boundary
$\mathcal{W}$	solution function space for pressure
$\mathcal{V}_h^v$	subspace of $\mathcal{V}^v$
$\mathcal{V}_h^0$	subspace of $\mathcal{V}^0$
$\mathcal{W}_h$	subspace of $\mathcal{W}$
$(\cdot, \cdot)$	$L^2(\Omega)$-inner product
$(\cdot, \cdot)$	$L^2(E)$-inner product over the element
E	Element
w	weight factor
χ	exponent of weight
r	radius
Δz_i	size of layer
N	number of layers
q	growth ratio for geometric layering

List of Figures

List of Tables

1 Introduction

1.1 Background

Antarctica is the fifth largest continent in the world, and approximately 98 % of it is covered by ice, the average thickness being about 2 km, and the ice sheets cover an area of about 14×10^6 km^2. It is in average also the driest, coldest and most windy place on Earth. The average precipitation is less than 2.5 cm annually (Greve & Blatter, 2009).

Because of these extreme conditions, Antarctica plays an important role in the global climate system, and it is important to understand the dynamics of the glaciers in Antarctica in the present and in the past.

The ice cores in Antarctica provide researchers with extremely valuable data of the climate history. The central and currently interesting questions are:

- What effect does the changing climate have on the glaciers in the polar regions?
- How fast will the see level rise because of these changes?
- How will these changes affect the global environment?

The main objective of this study is to improve our understanding of the local wind fields in the Scharffenbergbotnen (SBB) glacier, Antarctica. Especially to understand their effect on the so called Blue Ice Areas (BIAs), which cover about $0.8 - 1.6$ % of the entire surface area of Antarctica. A BIA is an area where the ice surface is clear of snow, and therefore reflects a blueish color (Bintanja, 1999; Sinisalo, 2007).

The BIAs can be of special interest when studying climate changes because many of them have very old layers of ice at the surface, and they may therefore provide paleoclimatological data that cannot be found anywhere else (Sinisalo, 2007; Grinsted, 2006). In fact, most of the BIAs are located close to hills and mountains, where the ice sheets tend to creep up along the mountain slopes towards the surface. This tendency is further explained in Figure 1.

Antarctica is the only place on Earth were one can find these BIAs, which are believed to exist because of the extreme conditions, such as high elevations, local topography, katabatic winds, low temperatures and little precipitation. Katabatic winds originate from temperature differences, leading to a cold and more dense air mass to fall down the mountain slopes at very high velocities (Sinisalo, 2007; Grinsted, 2006).

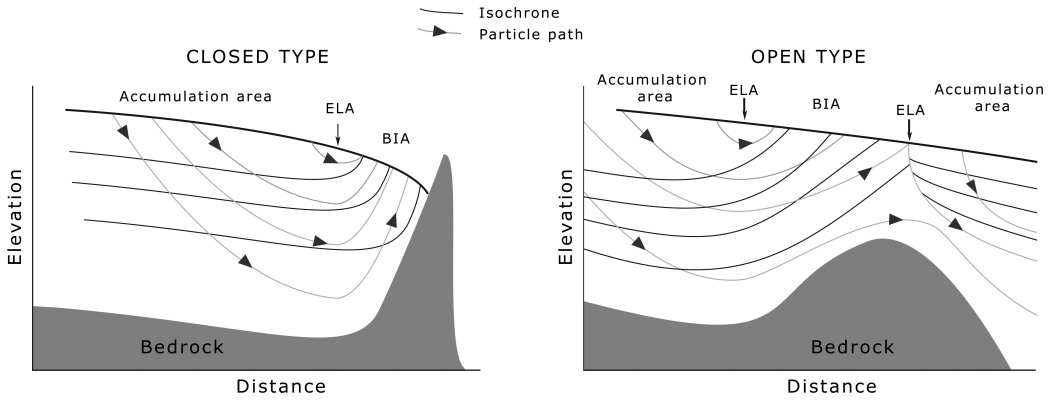

Figure 1: Stagnation ice flow at the end of a valley is shown in the left Figure. The right Figure shows an upward flow induced by an obstacle. ELA stands for the equilibrium line altitude, which acts as a separation line between the snow covered accumulation area and the ablation area, namely the BIA. An isochrone represents an individual annual layer, which creeps up towards the surface of the BIA. This leads to a near-vertical formation of the annual layers. (Figures taken from Sinisalo, 2007)

In this thesis the focus will be on using the Finite Element Method (FEM) with a suitable turbulence method for simulating the local wind fields in SBB. This study is not directly connected to the dynamics of the ice or the change in climate. We rather present the results of a simulation which aims to provide valuable information on how the snow is removed depending on local wind fields in the SBB area. Antarctica and the location of SBB is shown in Figure 2.

A photo of the mountains surrounding a blue ice area (bare glacier ice) in SBB is presented in Figure 3, where the accumulated snow along the mountain slope is also clearly visible. A rough outline of the area shown in Figure 3 and the BIAs is presented in Figure 4[1].

The horizontal wind data points used for defining parts of the boundary conditions of the model with respect to the Digital Elevation Model (DEM) (© Bundesamt für Kartographie und Geodäsie, Frankfurt am Main, http://www.bkg.bund.de) and the restricted area of our model are presented in Figure 6 in UTM29C coordinates.

[1]Northing stands for the distance to the equator, where locations that lie north of the equator are assigned a value of 0 meters at the equator. In order to avoid negative numbers, locations south of the equator are given a value of 10,000,000 meters at the equator, and the northing value reduces towards the South Pole. Easting on the other hand is the distance in a eastward direction from a reference point to the meridian that is specifically defined for the Universal Transverse Mercator (UTM) zones. This concept is explained in Figure 5.

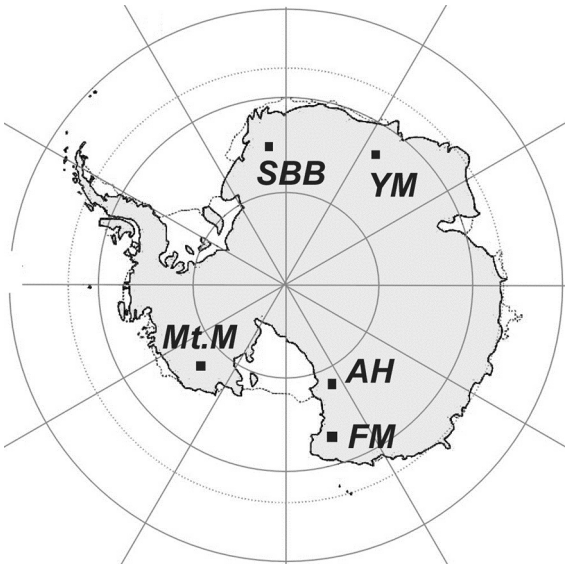

Figure 2: The location of Scharffenbergbotnen (SBB) in Antarctica. The figure also shows other BIAs of scientific interest, where YM indicates the Yamato Mountains, Mt.M = Mt. Moulton, AH = Allan Hills and FM stands for the Frontier Mountain. (Figure taken from Sinisalo, 2007)

Figure 3: The mountains surrounding Scharffenbergbotnen's Blue Ice Area. The accumulated snow along the mountain slope is also clearly visible. (Figure taken from Sinisalo, 2007)

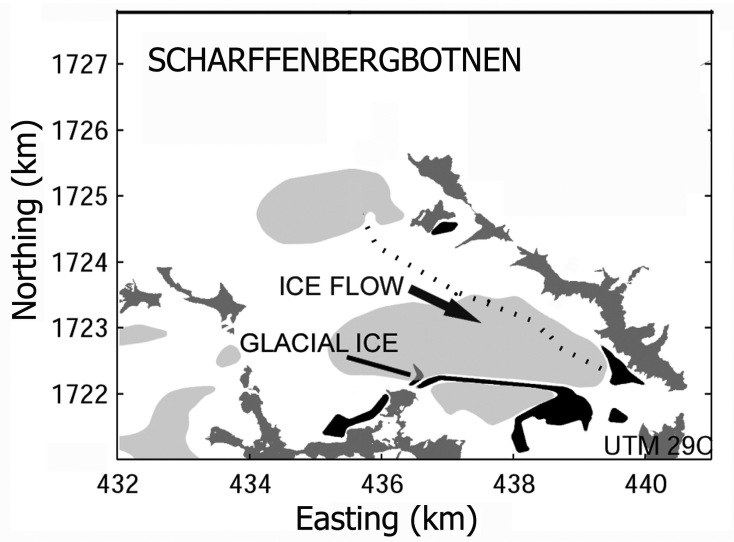

Figure 4: The Scharffenbergbotnen area, with the location of the Blue Ice Areas (light gray), exposed rocks on top of hills and mountains (dark gray) and moraines (black). (Figure taken from Sinisalo, 2007)

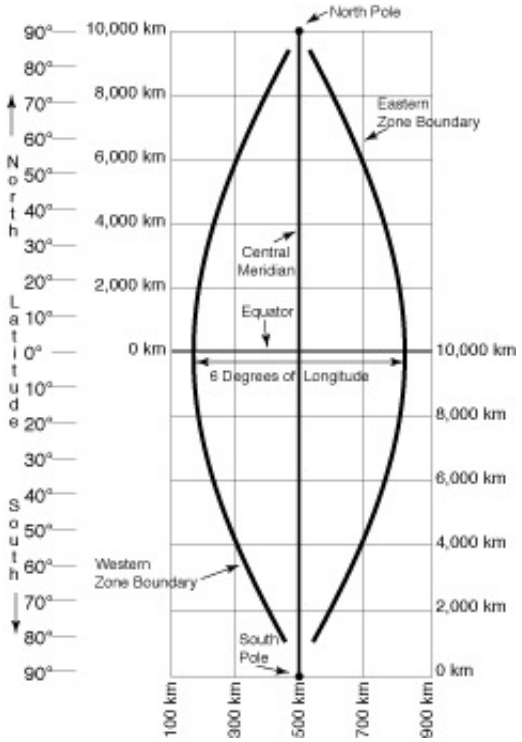

Figure 5: Description of northing and easting.
(Figure taken from http://www.maptools.com/UsingUTM/UTMdetails.html)

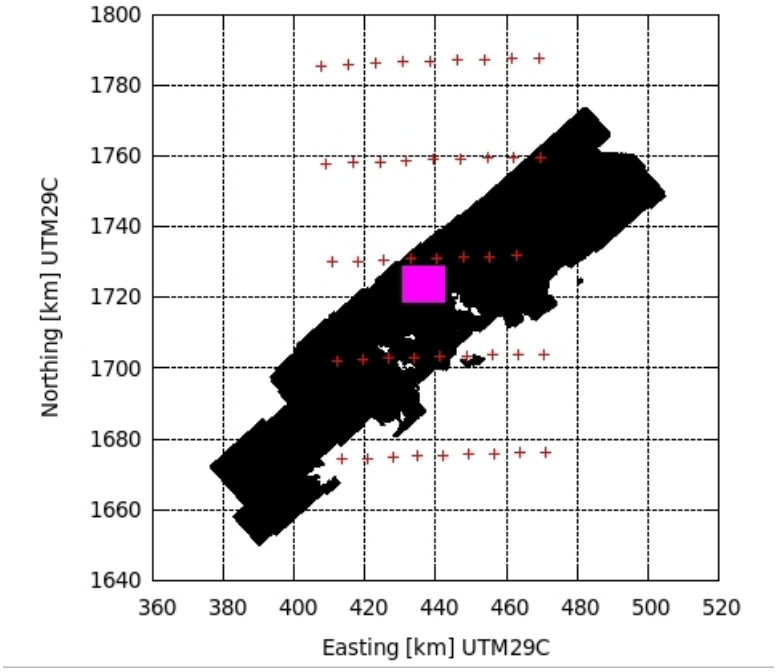

Figure 6: Alignment of the horizontal wind data points (red crosses) in relation to the DEM (black dots) and the restricted model area (pink dots) in the UTM29C coordinate frame.

1.2 Focus of the thesis and Large Scale Computational Fluid Dynamics

A Large Scale Computational Fluid Dynamics (LSCFD) finite element code ELMER (http://www.csc.fi/english/pages/elmer) is used to resolve the local wind fields in the SBB area, and thus make it possible to investigate the snow re-distribution patterns. The main focus will still be on resolving the wind field patterns and not the actual re-distribution of the snow.

Due to the chaotic nature of turbulence, the analysis and modeling of such flows is anything but straight forward. However, because of powerful supercomputers, the field of computational fluid dynamics has grown and made it possible to numerically solve complex flows. A transient simulation with the newly developed Variational Multiscale method (VMS) (Bazilevs *et al.* , 2008) is used to model the turbulent flow above the SBB glacier. The VMS method has been introduced as a powerful tool for solving computational problems where a large range of scales have to be dealt with, like our simulation where the flow becomes turbulent at larger Reynolds numbers (Bazilevs *et al.* , 2008; Rautaheimo, 2001). The VMS-method is therefore suitable for turbulent flow problems where the Direct Numerical Simulation (DNS)

is not feasible (Bazilevs *et al.* , 2008).

A turbulent flow includes swirls and eddies of different sizes which are caused when the turbulent kinetic energy is transferred down the turbulence energy cascade. The size ratio between these eddies can be large, and this is one of the main problems when solving LSCFD problems involving high Reynolds numbers (Rautaheimo, 2001). In order to resolve all the scales, one should use a very fine grid spacing which for many cases will not be feasible to compute. Thus, many turbulent models, involving empirical parameters and assumptions on how to model a flow without solving all the scales, have been established.

1.3 Problem setup

ELMER has been intensively used in ice sheet simulations (Zwinger & Moore, 2009; Gillet-Chaulet *et al.* , 2006) and it is currently also applied to the ice flow in SBB (based on communications with Dr. Thomas Zwinger (CSC — IT Center for Science, Finland) and John Moore, Professor of Global Change and Earth System Science (University of Lapland and Beijing Normal University)). This and the newly implemented VMS method gave us the motivation to also study the wind fields in SBB by using ELMER, and hence the FE-method.

In our model we make the assumptions that by choosing suitable boundary conditions and initial conditions we may restrict the area to contain only the valley and its surrounding mountains. This is, however, a very difficult task for an area like the one we are dealing with. Many problems arise, namely:

- How high should the model be extruded in order to avoid having the effects of the top boundary conditions interfere with the flow at the lower part of the model?

- How big a model should be used in order to resolve the flow in the area of interest, and what effect will a reduced model domain have on the results?

- How should the inflow, outflow and other boundary conditions be chosen in order to get a valid simulation and achieve convergence? The difficulty of choosing the initial and boundary conditions will be discussed in more detail in Section 2.

Since the VMS method used in ELMER does not have a suitable solver implemented for compressible flows, an incompressible solver will be used in this work.

The formation of katabatic winds is caused by temperature differences and the resulting flow of heavier, cold air along the flanks of the ice sheet. By imposing incompressibility, we ignore this effect inside the valley. This, nevertheless, is justified, as SBB resides on the margin of the ice sheet and the katabatic winds reaching the valley are formed hundred kilometers inland (van As & van den Broeke, 2006). Hence it is justified to ignore the density effects inside the valley and prescribe the katabatic winds as an incoming wall bounded jet entering the domain via its boundaries.

The goal of this thesis is to get an understanding on whether the local winds combined with the katabatic winds that occur in these areas can achieve the strengths to clear the BIAs (of the usually forming densifying snow layer that accumulates on the ice) . This is, however, rather a proof of concept and the research is considered qualitative.

Many assumptions have been made and the ERA-interim wind data (Berrisford *et al.* , 2009) provided information only on the average wind speeds and directions around SBB, but it does not contain information on temporal storms or local katabatic winds. Therefore the assumptions of the katabatic winds in the area were formed only on references (Luijting, 2009; Parish & Cassano, 2003; Zammett & Fowler, 2006) that describe the general nature and profiles of these winds. The direction of the katabatic winds used in this thesis is based on examining the DEM of the surrounding area (assuming that the direction is aligned with the steepest gradient of the upstream terrain) and discussions with Dr. Anna Sinisalo (University of Oslo).

In Section 2 the incompressible Navier-Stokes equations that describe the flow are explained. The basics of turbulence modeling along with a formulation of the VMS method are presented in Section 3, followed by the Sections Model Mesh and Model Setup. We introduce the wind data that we used for setting the boundary conditions of the FEM-model in Section 6. The results are presented in Section 7, followed by the conclusions in Section 8.

2 Navier-Stokes equations

The Navier-Stokes equations (NSE) were derived by the French mathematician L.M.H. Navier (1785-1836) and the British mechanican G. G. Stokes (1819-1903) by directly applying Newton's second law to the motion of a fluid, and adding the assumptions that the total stress acting on a fluid particle is the sum of a diffusing viscosity times strain and an isotropic pressure (Rautaheimo, 2001).

For a Newtonian fluid in plain shear flow the shear stress τ is linearly dependent on the strain rate $\frac{du}{dy}$ by the following equation

$$\tau = \mu \frac{du}{dy}, \tag{1}$$

where $\frac{du}{dy}$ is the velocity gradient perpendicular to the direction of shear and μ is the viscosity.

The Navier-Stokes equations describe the flow of a fluid, and for an incompressible flow the solution of these equations yield the velocity and the pressure of the fluid at a given point and time.

The concept of a continuum was first introduced by the French mathematician A. L. Cauchy in the 19th century. The modeling of a fluid or a solid as a continuum made it possible to deal with field variables, and the idea is that the object (fluid or solid) fills the space completely and no discontinuity exist. Further, a continuum should be continually sub-dividable into infinitesimal elements that have the same properties as those of the parent material or element.

In this chapter the incompressible Navier-Stokes equations are derived from the fundamental physical laws, *i.e.* conservation of mass, and conservation of momentum. We will first present them in the form of continuum mechanics and then derive from these laws the differential equations describing the behavior of fluid flows. The material properties are then used to describe the constitutive equations and relations.

2.1 The description of velocity

In fluid mechanics the Eulerian description of velocity is usually used, meaning that one is observing the flow from a fixed observers point of view (Layton, 2008; Batchelor, 2000), namely the velocity is expressed as a function of the fixed spatial coordinates x, y, z and the time t.

An alternative way to look at motion would be the Lagrangian way (Layton, 2008; Batchelor, 2000). There the velocity depends on the material coordinates X,

Y,Z and the time, meaning that the motion is observed by following the path of an individual fluid particle as it moves through space and time (the observer is moving with the flow).

The concept of velocity is described in Figure 7, where $\vec{u}_m$ denotes the velocity of the control volume $V(t)$ at time t and $\vec{u}$ denotes the flow velocity.

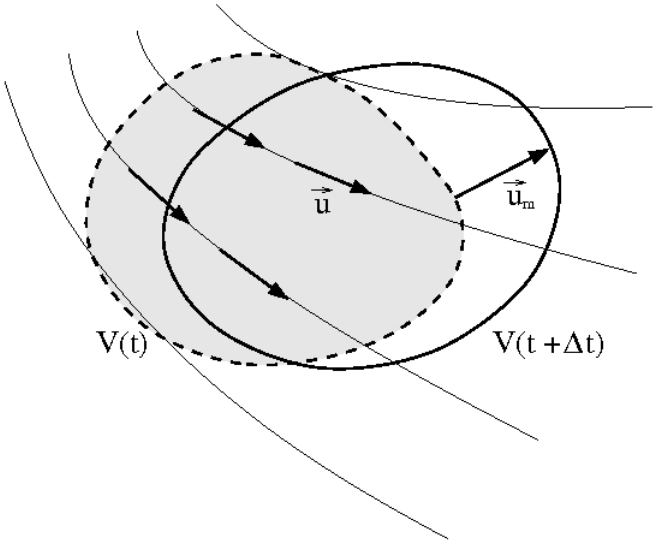

Figure 7: The description of velocity, where $V(t)$ describes the control volume at time t, and $V(t + \Delta t)$ describes the control volume at time $t + \Delta t$.

The Eulerian and Lagrangian descriptions are as follows:

$$\text{Euler: } \vec{u}_m \equiv \vec{0},$$

$$\text{Lagrange: } \vec{u}_m \equiv \vec{u}|_{\partial V(t)},$$

where $\partial V(t)$ is the boundary of the control volume.

2.2 The divergence theorem

The divergence theorem in vector form is

$$\int_{\partial V} \vec{n} \cdot \vec{u}(\vec{x}, t)\, dS = \int_V \nabla \cdot \vec{u}(\vec{x}, t)\, dV. \tag{2}$$

The divergence theorem states that the flux of any vector field $\vec{u}(\vec{x},t)$ out through a "closed" surface ∂V equals the volume integral of the divergence inside the surface.

The divergence of a tensor $\nabla \cdot \bar{\bar{\tau}}$ in an arbitrary orthonormal frame $\{\vec{e}_i\}$ is by Einstein notation $\tau_{ij,j}(\vec{x})\vec{e}_i$, where the subscripts ij,j denote the partial derivative of the ij component with respect to j. This means that

$$(\nabla \cdot \bar{\bar{\tau}})_i = (\sum_{j=1}^{3} \frac{\partial \tau_{ij}}{\partial x_j})\, \vec{e}_i.$$

The divergence theorem for tensors is

$$\int_{\partial V} \bar{\bar{\tau}} \vec{n}\, dS = \int_V \nabla \cdot \bar{\bar{\tau}}\, dV. \tag{3}$$

2.3 The transport theorem

The transport theorem also known as the Reynolds transport theorem (O. Reynolds (1842 - 1912)) states that

$$\frac{d}{dt}\int_{V(t)} \vec{G}(\vec{x},t)\, dV = \int_{V(t)} \frac{\partial}{\partial t}\vec{G}(\vec{x},t)\, dV + \int_{\partial V(t)} \vec{G}(\vec{x},t)(\vec{n}\cdot\vec{u})\, dS, \tag{4}$$

for a vector field $\vec{G}$. This means that the total change from the initial state inside a volume $V(t)$ equals the local change plus the flux trough the surface.

2.4 The Cauchy stress tensor

The stress acting on a volume inside of a continuum is described by the Cauchy stress tensor $\bar{\bar{\sigma}}$. This is usually divided into two tensors, namely the isotropic part $p\bar{\bar{I}}$, and the anisotropic part $\bar{\bar{\mathbb{T}}}$, which describes the deviatoric stress caused by the viscosity (Layton, 2008). Therefore we have

$$\bar{\bar{\sigma}} = -p\bar{\bar{I}} + \bar{\bar{\mathbb{T}}}, \tag{5}$$

where $\bar{\bar{I}}$ is the 3x3 identity matrix.

$$\bar{\bar{\sigma}} = \begin{pmatrix} \sigma_{11} & \sigma_{12} & \sigma_{13} \\ \sigma_{21} & \sigma_{22} & \sigma_{23} \\ \sigma_{31} & \sigma_{32} & \sigma_{33} \end{pmatrix}, \tag{6}$$

where σ_{ii}, with $i = 1, 2, 3$, denotes the normal stresses and σ_{ij}, with $i, j = 1, 2, 3$ and $i \neq j$, denotes the shear stresses.

The relation $\sigma_{ij} = \sigma_{ji}$ for all $i, j = 1, 2, 3$, where $i \neq j$ is due to the conservation of angular momentum, which will be explained later in this section. The relation states that the Cauchy stress tensor $\bar{\bar{\sigma}}$ is symmetric. The symmetry of the Cauchy stress tensor means that there are six independent stresses. The traction field on a surface with an outward normal $\vec{n}$ is given by

$$\vec{t} = \bar{\bar{\sigma}}\vec{n}. \tag{7}$$

2.5 Conservation of mass

The equation for the conservation of mass in a continuum

$$\frac{d}{dt}\int_{V(t)} \rho(\vec{x}, t)\, dV = 0, \tag{8}$$

states that the mass of the continuum in the control volume $V(t)$ does not change in time.

By applying the transport theorem (4) to Equation (8), the following form is obtained for the conservation of mass

$$\int_{V(t)} \frac{\partial \rho}{\partial t}\, dV + \int_{\partial V(t)} \rho(\vec{n} \cdot \vec{u})\, dS = 0. \tag{9}$$

Now by applying Gauss' theorem (2) to the above equation, an integral form of the equation integrated over the volume is obtained

$$\int_{V(t)} \left[\frac{\partial \rho}{\partial t} + \nabla \cdot (\rho \vec{u})\right] dV = 0. \tag{10}$$

Equation (10) holds for any volume $V(t)$, leading to the time-dependent differential equation

$$\frac{\partial \rho}{\partial t} + \nabla \cdot (\rho \vec{u}) = 0, \tag{11}$$

which has to be fulfilled. The equation states that the local change of density with respect to time $\frac{\partial \rho}{\partial t}$ is balanced by the convection $\nabla \cdot (\rho \vec{u})$. But since we are dealing with a constant density, $\rho =$ constant, this leads to the divergence of the velocity field to be zero

$$\nabla \cdot \vec{u} = 0. \tag{12}$$

2.6 Conservation of linear momentum

The principle of conservation of momentum is derived from Newton's second law, which states that the total force $\vec{F}$ acting on a body is equal to the temporal change $\frac{d}{dt}$ of its linear momentum $m\vec{u}$,

$$\vec{F} = \frac{d}{dt}(m\vec{u}). \tag{13}$$

Thus the conservation of momentum for a continuum approach leads to

$$\frac{d}{dt}\int_{V(t)} (\rho\vec{u})\, dV = \int_{\partial V(t)} \vec{t}\, dS + \int_{V(t)} \rho\vec{f}\, dV, \tag{14}$$

where $\vec{t}$ and $\vec{f}$ represent surface and body forces respectively.

By applying Reynolds transport theorem (4) to the vector $\rho\vec{u}$ we get

$$\int_{V(t)} \frac{\partial(\rho\vec{u})}{\partial t}\, dV + \int_{\partial V(t)} (\rho\vec{u})(\vec{n}\cdot\vec{u})\, dS = \int_{\partial V(t)} \vec{t}\, dS + \int_{V(t)} \rho\vec{f}\, dV. \tag{15}$$

The outer product is defined as

$$\vec{a}\otimes\vec{b} = \begin{pmatrix} a_1b_1 & a_1b_2 & a_1b_3 \\ a_2b_1 & a_2b_2 & a_2b_3 \\ a_3b_1 & a_3b_2 & a_3b_3 \end{pmatrix}, \tag{16}$$

where $\vec{a} = (a_1, a_2, a_3)^T$, $\vec{b} = (b_1, b_2, b_3)^T$ and the notation $(\cdot)^T$ represents the transpose.

By applying the definition of the outer product (16) and the divergence theorem for tensors (3) to the term $(\rho\vec{u})(\vec{n}\cdot\vec{u}) = \rho(\vec{u}\otimes\vec{u})\vec{n}$ in equation (15), it may be written as

$$\int_{\partial V(t)} \rho(\vec{u}\otimes\vec{u})\vec{n}dS = \int_{V(t)} \nabla\cdot((\rho\vec{u})\otimes\vec{u})dV. \tag{17}$$

Since ρ is constant the term $\nabla\cdot((\rho\vec{u})\otimes\vec{u})$ in (17) becomes

$$\nabla\cdot((\rho\vec{u})\otimes\vec{u}) = \rho\nabla\cdot(\vec{u}\otimes\vec{u}). \tag{18}$$

Due to the definition of the outer product (16) and (12) we write

$$\nabla\cdot(\vec{u}\otimes\vec{u}) = (\vec{u}\cdot\nabla)\vec{u} + \underbrace{(\nabla\cdot\vec{u})\vec{u}}_{=0} = (\vec{u}\cdot\nabla)\vec{u}. \tag{19}$$

The other surface integral in equation (15) becomes by using the divergence theorem for tensors (3) and the definition of the traction field (7)

$$\int_{\partial V(t)} \vec{t} dS = \int_{V(t)} \nabla \cdot \bar{\bar{\sigma}} dV. \tag{20}$$

Substitution of equations (17) and (20) into equation (15) leads to

$$\int_{V(t)} \rho \left[\frac{\partial \vec{u}}{\partial t} + \nabla \cdot (\vec{u} \otimes \vec{u}) \right] dV = \int_{V(t)} \left[\nabla \cdot \bar{\bar{\sigma}} + \rho \vec{f} \right] dV. \tag{21}$$

Since this must hold for every $V(t)$, we get

$$\rho(\frac{\partial \vec{u}}{\partial t} + \nabla \cdot (\vec{u} \otimes \vec{u})) = \nabla \cdot \bar{\bar{\sigma}} + \rho \vec{f}. \tag{22}$$

Using (19) we obtain

$$\rho(\frac{\partial \vec{u}}{\partial t} + (\vec{u} \cdot \nabla)\vec{u}) - \nabla \cdot \bar{\bar{\sigma}} = \rho \vec{f}. \tag{23}$$

2.7 Conservation of angular momentum

The conservation of angular momentum for a continuum is

$$\frac{d}{dt} \int_{V(t)} \vec{r} \times (\rho \vec{u}) \, dV = \int_{\partial V(t)} \vec{r} \times \vec{t} \, dS + \int_{V(t)} \vec{r} \times \rho \vec{f} \, dV, \tag{24}$$

where $\vec{r}$ is the position vector from the origin $\vec{0}$ to the position coordinate $\vec{x}$, meaning that $\vec{r} = \vec{x} - \vec{0}$. The surface integral in equation (24) can by applying the divergence theorem for tensors (3) along with the relation (7) be expressed as a volume integral

$$\int_{\partial V(t)} \vec{r} \times \vec{t} \, dS = \int_{V(t)} \nabla \cdot (\vec{r} \times \bar{\bar{\sigma}}) \, dV. \tag{25}$$

By applying the theorem (4) to the lefthand side of equation (24) we get

$$\frac{d}{dt} \int_{V(t)} \vec{r} \times (\rho \vec{u}) \, dV = \int_{V(t)} \frac{\partial (\vec{r} \times (\rho \vec{u}))}{\partial t} \, dV + \int_{\partial V(t)} (\vec{r} \times \rho \vec{u}) \vec{n} \cdot \vec{u} \, dS. \tag{26}$$

Using (2) we get the following form of the surface integral in (26)

$$\int_{\partial V(t)} (\vec{r} \times \rho \vec{u}) \vec{n} \cdot \vec{u} \, dS = \int_{V(t)} \nabla \cdot [(\vec{r} \times \rho \vec{u}) \otimes \vec{u}] dV., \tag{27}$$

which leads to equation (26) taking the following form

$$\frac{d}{dt}\int_{V(t)} \vec{r}\times(\rho\vec{u})\,dV = \int_{V(t)} \frac{\partial(\vec{r}\times(\rho\vec{u}))}{\partial t}\,dV + \int_{V(t)} \nabla\cdot[(\vec{r}\times\rho\vec{u})\otimes\vec{u}]dV. \tag{28}$$

By insertions of (28) and (25) into (24) we get

$$\int_{V(t)} \frac{\partial(\vec{r}\times(\rho\vec{u}))}{\partial t}\,dV + \int_{V(t)} \nabla\cdot[(\vec{r}\times\rho\vec{u})\otimes\vec{u}]dV = \int_{V(t)} \nabla\cdot(\vec{r}\times\bar{\bar{\sigma}})\,dV + \int_{V(t)} \vec{r}\times\rho\vec{f}\,dV, \tag{29}$$

which must hold for all $V(t)$, leading to

$$\frac{\partial(\vec{r}\times(\rho\vec{u}))}{\partial t} + \nabla\cdot[(\vec{r}\times\rho\vec{u})\otimes\vec{u}] = \nabla\cdot(\vec{r}\times\bar{\bar{\sigma}}) + \vec{r}\times\rho\vec{f}. \tag{30}$$

Equation (30) expressed in index notations reads

$$\frac{\partial}{\partial t}(\rho\varepsilon_{ijk}r_j u_k) + (\rho\varepsilon_{ijk}r_j u_k u_l)_{,l} = (\varepsilon_{ijk}r_j\sigma_{kl})_{,l} + \varepsilon_{ijk}r_j\rho f_k, \tag{31}$$

where ε_{ijk} is the Levi-Civita symbol, which is defined as follows

$$\varepsilon_{ijk} = \begin{cases} 1 & \text{if} \quad (i,j,k) \text{ is } (1,2,3),\ (2,3,1) \text{ or } (3,1,2), \\ -1 & \text{if} \quad (i,j,k) \text{ is } (1,3,2),\ (3,2,1) \text{ or } (2,3,1), \\ 0 & \text{if} \quad i=j,\ i=k \text{ or } j=k. \end{cases}$$

The equation for conservation of momentum (23) is used to simplify the above expression. Applying the cross product $\vec{r}\times$ from the left-hand side to (23) and denoting in index notation, we obtain

$$\begin{aligned} &\frac{\partial}{\partial t}(\rho\varepsilon_{ijk}r_j u_k) + r_j(\rho\varepsilon_{ijk}u_k u_l)_{,l} = r_j(\varepsilon_{ijk}\sigma_{kl})_{,l} + \varepsilon_{ijk}r_j\rho f_k. \\ \Rightarrow\ &\frac{\partial}{\partial t}(\rho\varepsilon_{ijk}r_j u_k) + (\rho\varepsilon_{ijk}r_j u_k u_l)_{,l} - \rho\varepsilon_{ijk}u_k u_l r_{j,l} \\ &\qquad = (\varepsilon_{ijk}r_j\sigma_{kl})_{,l} - \varepsilon_{ijk}\sigma_{kl}r_{j,l} + \varepsilon_{ijk}r_j\rho f_k. \end{aligned} \tag{32}$$

By substracting equation (32) from (31) we get

$$\begin{aligned}
&\rho\varepsilon_{ijk}u_k u_l\delta_{jl} = \varepsilon_{ijk}\sigma_{kl}\delta_{jl} \\
&\Rightarrow \rho\varepsilon_{ijk}u_k u_j = \varepsilon_{ijk}\sigma_{kj} \\
&\Rightarrow \tfrac{1}{2}(\rho\varepsilon_{ijk}u_k u_j + \rho\varepsilon_{ikj}u_j u_k) = \tfrac{1}{2}(\varepsilon_{ijk}\sigma_{kj} + \varepsilon_{ikj}\sigma_{jk}) \\
&\Rightarrow \rho\varepsilon_{ijk}(u_k u_j - u_j u_k) = \varepsilon_{ijk}(\sigma_{kj} - \sigma_{jk}) \\
&\Rightarrow \varepsilon_{ijk}(\sigma_{kj} - \sigma_{jk}) = 0.
\end{aligned}$$

For $i = 1$ this leads to

$$\begin{aligned}
&\varepsilon_{123}(\sigma_{32} - \sigma_{23}) + \varepsilon_{132}(\sigma_{23} - \sigma_{32}) = 0 \\
&\Rightarrow \sigma_{32} = \sigma_{23}.
\end{aligned}$$

For $i = 2$ and $i = 3$ we get $\sigma_{13} = \sigma_{31}$ and $\sigma_{12} = \sigma_{21}$ respectively, which implies that the Cauchy stress tensor is symmetric due to the conservation of angular momentum.

2.8 Constitutive equations

For a Newtonian compressible fluid equation (5) becomes (Layton, 2008)

$$\bar{\bar{\sigma}} = 2\mu\bar{\bar{\varepsilon}} - \frac{2}{3}\mu(\nabla\cdot\vec{u})\bar{\bar{I}} - p\bar{\bar{I}}, \tag{33}$$

where μ is the viscosity of the fluid, and the coefficient $-\frac{2}{3}\mu$ originates from the Stokes hypothesis for compressible flow. $\bar{\bar{\varepsilon}}$ is the rate of strain tensor,

$$\varepsilon_{ij} = \frac{1}{2}(\frac{\partial u_i}{\partial x_j} + \frac{\partial u_j}{\partial x_i}). \tag{34}$$

Due to divergence free velocity field (12) of an incompressible flow we write (33) as

$$\bar{\bar{\sigma}} = 2\mu\bar{\bar{\varepsilon}} - p\bar{\bar{I}}, \tag{35}$$

2.9 The incompressible Navier-Stokes equations with initial and boundary conditions

Using condition (12) and by substituting (35) into (23) we get the incompressible Navier-Stokes equations

$$\nabla \cdot \vec{u} = 0 \qquad \text{in } \Omega \text{ for } t \in (0, T) \tag{36}$$

$$\frac{\partial \vec{u}}{\partial t} + (\vec{u} \cdot \nabla)\vec{u}) + \nabla p - 2\mu \nabla \bar{\bar{\varepsilon}}(\vec{u}) = \vec{f} \qquad \text{in } \Omega \text{ for } t \in (0, T). \tag{37}$$

The initial condition describes the velocity as vector components and the pressure as a scalar inside the model domain. This is done by setting the conditions to

$$\vec{u} = \vec{u}_0 \qquad \text{in } \Omega \text{ for } t = 0, \tag{38}$$

where Ω is the model domain.

The Dirichlet boundary condition imposed on a Partial Differential Equation (PDE), describes the values a solution needs to take on the boundary of the domain. For the NSE this means setting the velocity on the boundary $\partial\Omega$.

Dirichlet boundary condition:

$$\vec{u}\,|_{\partial\Omega} = \vec{v}. \tag{39}$$

The Neumann boundary condition implemented on a PDE on the other hand specifies the values of the derivative of the solution on the boundary.

Neumann boundary condition:

$$\bar{\bar{\sigma}}\vec{n}\,|_{\partial\Omega} = \vec{t}. \tag{40}$$

The mixed boundary conditions used in our work are described partly as Dirichlet and partly as Neumann boundary conditions.

Mixed boundary condition:

$$\vec{u} \cdot \vec{n}\,|_{\partial\Omega} = 0, \tag{41}$$

and

$$(\bar{\bar{\sigma}}\vec{n} - ((\bar{\bar{\sigma}}\vec{n}) \cdot \vec{n})\vec{n})\,|_{\partial\Omega} = \vec{0}. \tag{42}$$

It is important to understand that the closer the boundary condition is to the area of interest, the more crucial it is to set the boundary condition as correctly as possible.

The strong non-linearity with respect to the velocity $(\vec{u} \cdot \nabla)\vec{u}$ in the acceleration

term of the partial differential equation (37) is the cause of turbulence and the main source of problems for numerical solutions of the Navier-Stokes equations.

Problems also arise when trying to define the initial and boundary conditions, at least when dealing with more complex models, like the one discussed in this work. The problem with turbulence modeling is that a careful and physically reasonable description of the initial and boundary conditions does not guarantee a solution. This is because numerical instabilities occur very easily in turbulence modeling, due to the dominating nonlinear convection term. The large range of scales in turn leads to extremely high computational costs if one is trying to achieve a solution by a DNS approach.

3 The Variational Multiscale method and turbulence modeling

Under laminar conditions the flow of a fluid is considered to be regular and smooth, but it does not have to be steady. Turbulent flow on the other hand is of chaotic nature, thus the flow paths are irregular and unsteady.

The modeling of turbulent flows is considered to be one of the most challenging areas in mathematics and Computational Fluid Dynamics (CFD), and no analytical solutions exist for any turbulent flows (Rautaheimo, 2001; Gravemeier, 2003). Therefore all the solutions have to be obtained numerically, which can cause problems in many cases. Numerous *ad hoc* models for turbulence have been created in order to solve such problems.

A Direct Numerical Simulation (DNS) where one tries to solve all the scales, is not a feasible option for several turbulent flow problems. Vortices are continually forming and breaking down, and size ratios exist in both laminar and turbulent flows. The ratio between the largest and smallest eddies increases rapidly with the Reynolds number, therefore making turbulent flows extremely costly to compute. The big eddies turn into smaller ones, and the smallest ones are then finally dissipated by the viscous forces at the Kolmogorov scale (Gravemeier, 2003; Rautaheimo, 2001).

Because of these size ratios the flow usually needs to be approximated by suitable turbulence models, and *ad hoc* functions which are based on empirical information and may not be suitable for all types of flows (Rodi, 1984).

Many numerical approaches exist for resolving the scalars and vectors in turbulent flows, such as the time-averaging Reynolds Averaged Navier-Stokes (RANS) models and other theoretical frameworks, where the basic concept is to resolve the large eddies, and then to model the effect that the small eddies have on these larger eddies by using *ad hoc* models based on experimental values and equations.

Some methods worth mentioning are the RANS equations with for example the k-ϵ-model (which solves the k and ϵ equations) and the $V2F$-model (which is a four equation relaxation model, solving not only the k and ϵ functions, but also the to the streamline perpendicular velocity fluctuations $V2$ and a global relaxation function f), Large Eddy Simulation (LES) and the VMS method. The VMS method will be described in detail, because of our approach to use only the recently introduced VMS-model (Hughes, 1995) for solving the flow.

Usually the results of these turbulence models are much smoother than the actual flow. However, what is lost in exactness of the solution is compensated in the

decreased computational cost. The main idea of using these approaches is to dramatically reduce the number of nodes needed for solving turbulent CFD problems (Rautaheimo, 2001; Gravemeier, 2003).

3.1 LES and VMS turbulence model

LES is an approach where only the large scales are resolved in their complete resolution, and the effect of the unresolved smaller scales on the flow is modeled. Hence, the LES approach allows to reduce the number of nodes needed compared to a DNS approach, and consequently also lowers the computational cost. This approach is widely used especially in meteorology, where the large-scale turbulent motions are of particular interest (John *et al.* , 2010).

The Variational Multiscale method (VMS) is an alternative method to the LES method. The main difference between VMS and LES is that the VMS method projects the scales into the function spaces rather than filtering them by spatial averaging. In this way the VMS-method avoids several problems including the problem of the spatial filtering and spatial differentiation not holding in bounded domains or for non-constant filter widths, and the problem of choosing the correct boundary conditions for the spatially averaged large scales, because these are not known (John *et al.* , 2010).

3.2 The mathematics behind the VMS framework

The VMS method (Bazilevs *et al.* , 2007) also known as the Stabilized Method (Hoffman & Johnson, 2006; Hoffman & Johnson, 2007), which is founded on the weak form of the Navier-Stokes equations, was used for modeling the flow above the SBB-area. A control of the equation residual is included in the method by using a weighted least squares term in the variational formulation, which leads to a automatic FEM turbulence model. The elements used in this work are continuous isoparametric hexahedrals.

The time-discretization of the Navier-Stokes equation (37) is

$$0 = t_0 < t_1 < t_2 .... < t_N = T,$$

where $n = 1, 2, 3, ..., N$, and

$$t_n = n\Delta t.$$

The backward Euler method

$$\frac{\partial \vec{u}}{\partial t} \approx \frac{\vec{u}^{\,n} - \vec{u}^{\,n-1}}{\Delta t} \tag{43}$$

is used for time stepping. This leads to the time-discretized form of equation (37)

$$\frac{\vec{u}^{\,n} - \vec{u}^{\,n-1}}{\Delta t} + (\vec{u}^{\,n} \cdot \nabla)\vec{u}^{\,n} - 2\mu \nabla \cdot \bar{\bar{\epsilon}}(\vec{u}^{\,n}) + \nabla p^n = \vec{f}^{\,n}, \tag{44}$$

where $\vec{u}^{\,n} = \vec{u}(t_n)$ and $\vec{f}^{\,n} = \vec{f}(t_n)$.

The boundary condition on the parts of $\partial\Omega$ where a Dirichlet condition is applied is

$$\vec{u}^{\,n}|_{\partial\Omega} = \vec{v} \tag{45}$$

and

$$\vec{u}^{\,n} \cdot \vec{n}\,|_{\partial\Omega} = 0 \tag{46}$$

on the parts where a mixed condition is used.

Before we introduce the variational formulation of the time-discretized Navier-Stokes equations we introduce the following notations: $(\cdot,\cdot)$ denotes the $L^2(\Omega)$ -inner product and $(\cdot,\cdot)_E$ denotes the $L^2(E)$ -inner products.

The variational formulation without the stabilization term is stated as follows: Find the pair $(\vec{u}^{\,n}, p^n) \in \mathcal{V}^v \times \mathcal{W}$ such that

$$(\frac{\vec{u}^{\,n} - \vec{u}^{\,n-1}}{\Delta t}, \vec{v}) + ((\vec{u}^{\,n} \cdot \nabla)\vec{u}^{\,n} + \nabla p^n, \vec{v}) - 2\mu(\bar{\bar{\epsilon}}(\vec{u}^{\,n}), \bar{\bar{\epsilon}}(\vec{v})) = (\vec{f}^{\,n}, \vec{v}), \tag{47}$$

$$\forall\, \vec{v} \in \mathcal{V}^0,$$

$$(\nabla \cdot \vec{u}^n, q) = 0 \qquad \forall\, q \in \mathcal{W},$$

where $\mathcal{V}^v$ is the space for which the solution satisfies the boundary condition (45) and $\mathcal{V}^0$ is the same space where $\vec{v} = 0$ on the boundary. $\mathcal{W}$ is the space for the pressure.

In order to solve equation (47) with the finite element method, the equation naturally has to be discretized into subspaces. Thus we choose the following subspaces:

$$\mathcal{V}_h^v \subset \mathcal{V}^v, \qquad \mathcal{V}_h^0 \subset \mathcal{V}^0 \qquad \text{and} \qquad \mathcal{W}_h \subset \mathcal{W},$$

which in turn leads to a problem for which we need to find $\vec{u}_h \in \mathcal{V}_h^v$ and $p_h \in \mathcal{W}_h$

such that

$$(\frac{\vec{u}_h^{\,n} - \vec{u}_h^{\,n-1}}{\Delta t}, \vec{v}) + ((\vec{u}_h^{\,n} \cdot \nabla)\vec{u}_h^{\,n} + \nabla p_h^n, \vec{v}) - 2\mu(\bar{\bar{\epsilon}}(\vec{u}_h^{\,n}), \bar{\bar{\epsilon}}(\vec{v})) = (\vec{f}^{\,n}, \vec{v}), \qquad (48)$$

$$\forall\, v \in \mathcal{V}_h^0,\, \forall\, q \in \mathcal{W}_h.$$

Equation (48) is stabilized by adding a stabilization term which leads to the following form

$$\begin{aligned}(\frac{\vec{u}_h^{\,n} - \vec{u}_h^{\,n-1}}{\Delta t}, \vec{v}) + ((\vec{u}_h^{\,n} \cdot \nabla)\vec{u}_h^{\,n} + \nabla p_h^n, \vec{v}) - 2\mu(\bar{\bar{\epsilon}}(\vec{u}_h^{\,n}), \bar{\bar{\epsilon}}(\vec{v})) \\ + \sum_E \delta_E((\vec{u}_h^{\,n} \cdot \nabla)\vec{u}_h^{\,n} + \nabla p^{\,n}, (\vec{u}_h^{\,n} \cdot \nabla)\vec{v} + \nabla q)_E \\ = (\vec{f}^{\,n}, \vec{v}) + \sum_E \delta_E(\vec{f}^{\,n}, (\vec{u}_h^{\,n} \cdot \nabla)\vec{v} + \nabla q)_E, \quad (49)\end{aligned}$$

$$\forall\, v \in \mathcal{V}_h^0,\, \forall\, q \in \mathcal{W}_h.$$

where the index E refers to an element and

$$\delta_E = (\frac{1}{\Delta t} + \frac{\vec{u}^{\,n}}{h_E})^{-1},$$

where h_E represents the size of element E.

Numerous test cases and examples for the VMS method can be found in various references such as: (Gravemeier, 2003; Gravemeier *et al.* , 2006; Bazilevs *et al.* , 2008).

4 Model mesh

The mesh for the model of the Scharffenbergbotnen area is presented in detail in this section. The area is modeled using an extrusion perpendicular from the surface to a fixed height covering the essential part of the Atmospheric Boundary Layer (ABL), which is the lower part of the troposphere, where the surface of the earth is considered to affect the flow through turbulent diffusion.

The mesh footprint was created by the mesh generation program GAMBIT and the extrusion and the vertical mesh layering was done by coding new features into the open source code ELMER. The scattered DEM data was used for calculation of the surface elevation of the footprint nodes. The detailed sequence of the pre-processing steps is explained in the following subsections.

4.1 SBB model: plain footprint mesh

The plane footprint mesh (in 2D) was created so that the characteristic length for the elements in the valley was chosen to be 50 meters, see the red line in Figure 8. The characteristic length at the surface boundaries was chosen to be 300 meters with a linear growth in element size from the line to the boundaries. Thus a finer horizontal resolution was achieved in the valley where it mattered the most. The 2D mesh consisted of 2552 bilinear rectangular surface elements and 2612 nodes, 118 of the elements were edge elements.

4.2 The extrusion of the plain footprint mesh

The elevation of each element node is calculated from the surrounding DEM points inside a radius R of 150 m. When evaluating the elevation of each node, the weight factor w for each point in the DEM was calculated by choosing a value of $\chi = 1.2$ for the contribution of weight and using the following equation for the weight factor

$$w = 1/r^{\chi}, \tag{50}$$

where r is the distance from the node to the data point. The elevation of a node is then calculated by the surrounding DEM data points inside the radius R by the inverse distance method

$$\varsigma_n = \frac{\Sigma_i^m \varsigma_i \cdot w_i}{m}, \tag{51}$$

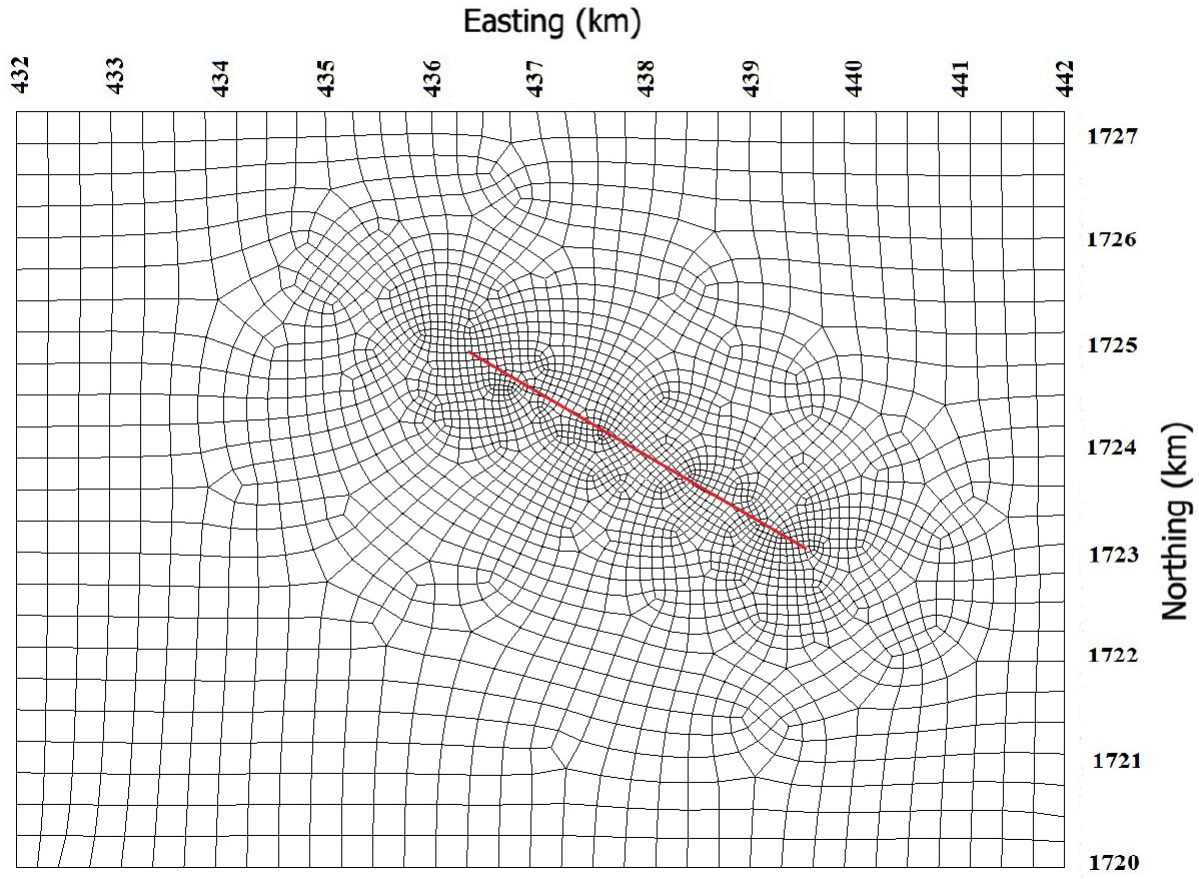

Figure 8: The mesh for the footprint of SBB, created by using the mesh generator program GAMBIT. The red line indicates the position where the characteristic length (50 meters) for the elements in the valley is applied. The characteristic length for the elements on the boundaries was chosen to be 300 meters.

where ς_n represents the calculated elevation value for the specific node, ς_i is the elevation value of the data point i and w_i is the weight factor for that specific data point in relation to the node location. A three-dimensional Figure of the DEM covering the model area is presented in Figure 9. The surface elevation of the model mesh is presented in Figure 10.

In order to create a mesh that works for the complex topology of Scharffenbergbotnen we used a geometric series to define the distance between the vertical layers. Uniform vertical layers would have lead to large computational costs or alternatively a mesh that would be too coarse near the surface. The size of a layer is Δz_i, where the subindex i represents the i^{th} layer.

Smaller layers were used near the surface to achieve high accuracy where it mat-

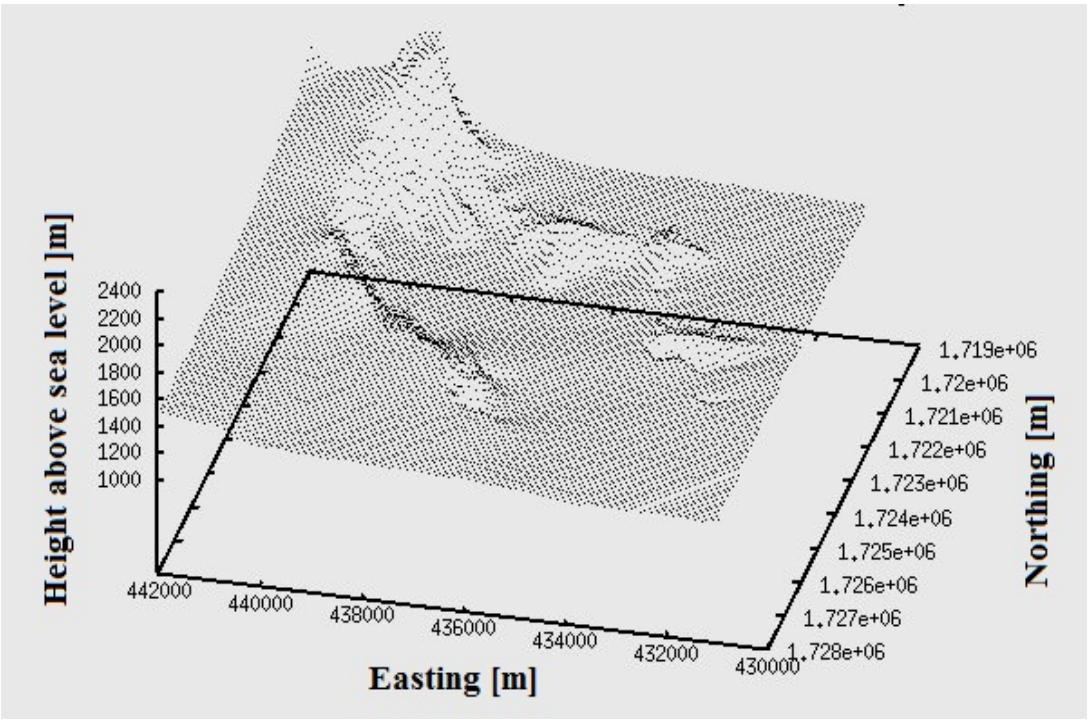

Figure 9: A three-dimensional plot of the DEM, with coordinates in the UTM29C zone. The elevation is expressed in meters above sea level.

tered the most. The geometric series for the vertical resolution was created so that the relation between the upper and lower layer is $\Delta z_N/\Delta z_1 = 10 = q^{N-1}$. The constant q is

$$q = \log_{10}^{-1}(\frac{1}{N-1}) = 10^{\frac{1}{N-1}}. \tag{52}$$

This means that at a given point $p_{i,j} = (x_p, y_p)$ the distance from the surface to the top of the model is the sum of the vertical layers at that given point. Namely $\sum_{i=1}^{N} \Delta z_i = h_t(p) - h_b(p)$, where N is the number of layers, and $h_b(p)$ is the elevation at the bottom at the point $p_{i,j}$, and $h_t(p)$ is the elevation at the top at the point $p_{i,j}$.

The geometric layering was accomplished by adapting an existing stand-alone open source code, namely the ExtudeMesh.c file, which is downloadable at (`http://www.elmerfem.org/wiki/index.php/ExtrudeMesh`).

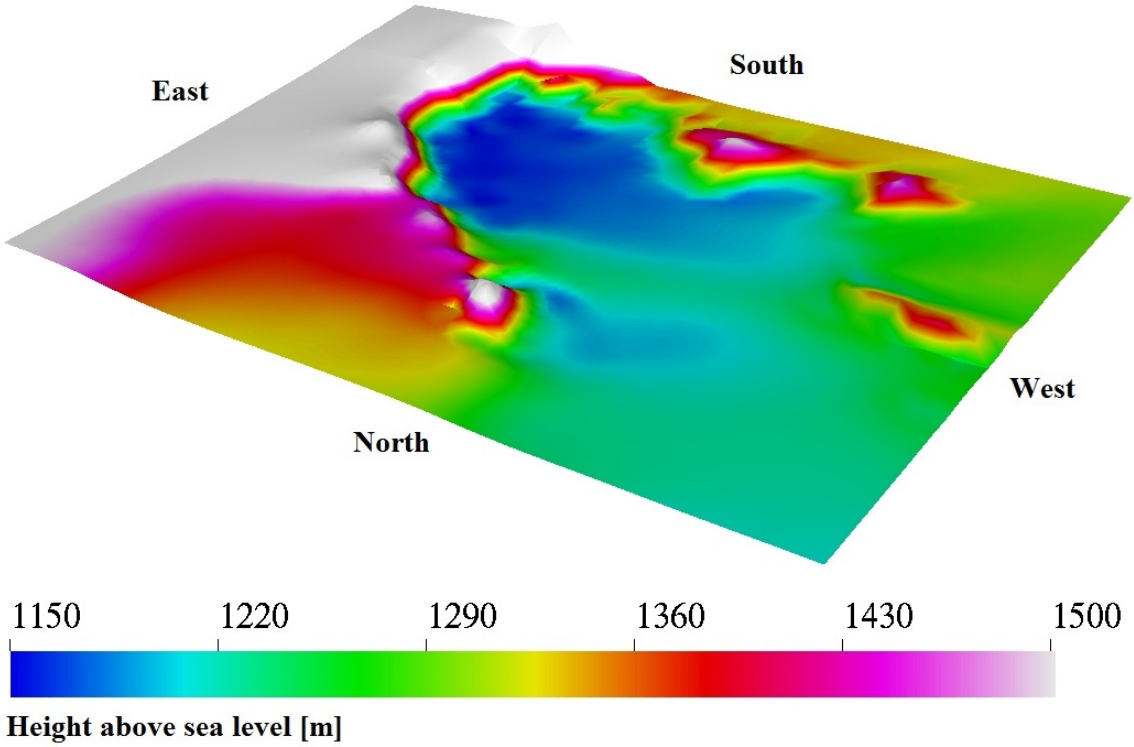

Figure 10: The bottom surface of the mesh, created from the DEM in Figure 9. The color scale shows the elevation up to 1500m above sea level, the white parts are elevations of more than 1500m.

4.2.1 3D Mesh: Extruded footprint with a uniform z-value of 2500 m at the top surface

The extrusion was chosen so that the upper surface of the model was at a uniform z-value of 2500 meters and 20% of the entire height was chosen to consist of the geometrically distributed layers, leading to a refinement with a thickness that depends on the horizontal position. The ratio for the geometrical layers was chosen to be $q = 1.05$. The number of boundary layers (geometrically distributed layers) was chosen to be 15, and the total number of layers to 25. The final 3D mesh consisted of 65300 nodes, 61248 elements, and 7936 boundary elements.

4.3 Definition of the model boundaries

The model domain and boundaries are defined as follows:

- Model domain Ω

- Model boundaries $\partial\Omega = \Gamma_E \bigcup \Gamma_W \bigcup \Gamma_N \bigcup \Gamma_S \bigcup \Gamma_{top} \bigcup \Gamma_{bed}$, where index E stands for east, W for west, N for of the north boundary, S for the south boundary, *top* stands for the upper surface with $z = 2500$m and *bed* stands for the lower surface, where $h = 0$.

The mesh boundaries are presented in Figures 11 to 13.

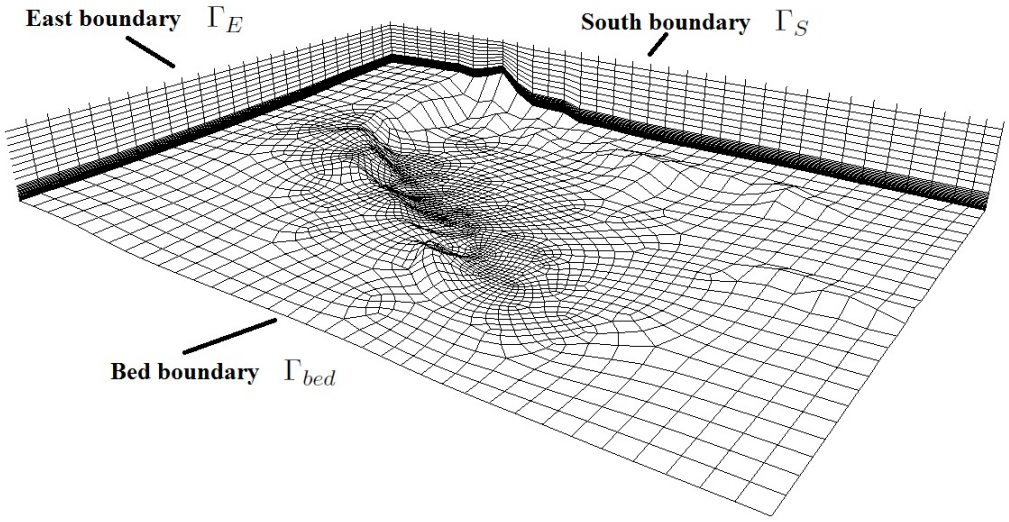

Figure 11: The lower surface, east boundary and the south boundary of the extruded mesh

The north, south and top boundaries where further split into subboundaries, namely $\Gamma_N = \Gamma_{N1} \bigcup \Gamma_{N2}$, $\Gamma_S = \Gamma_{S1} \bigcup \Gamma_{S2}$ and $\Gamma_{top} = \Gamma_{top1} \bigcup \Gamma_{top2}$.

The easting values (in UTM29C coordinates) for the boundaries where as follows:

$$\Gamma_{N1} = \{4.42 \times 10^5 \text{ km} > x > 4.41 \times 10^5 \text{ km}\},$$

$$\Gamma_{N2} = \{4.41 \times 10^5 \text{ km} > x > 4.32 \times 10^5 \text{ km}\},$$

$$\Gamma_{top1} = \{4.42 \times 10^5 \text{ km} > x > 4.41 \times 10^5 \text{ km}\},$$

$$\Gamma_{top2} = \{4.41 \times 10^5 \text{ km} > x > 4.32 \times 10^5 \text{ km}\},$$

$$\Gamma_{S1} = \{4.42 \times 10^5 \text{ km} > x > 4.39 \times 10^5 \text{ km}\},$$

and

$$\Gamma_{S2} = \{4.39 \times 10^5 \text{ km} > x > 4.32 \times 10^5 \text{ km}\}.$$

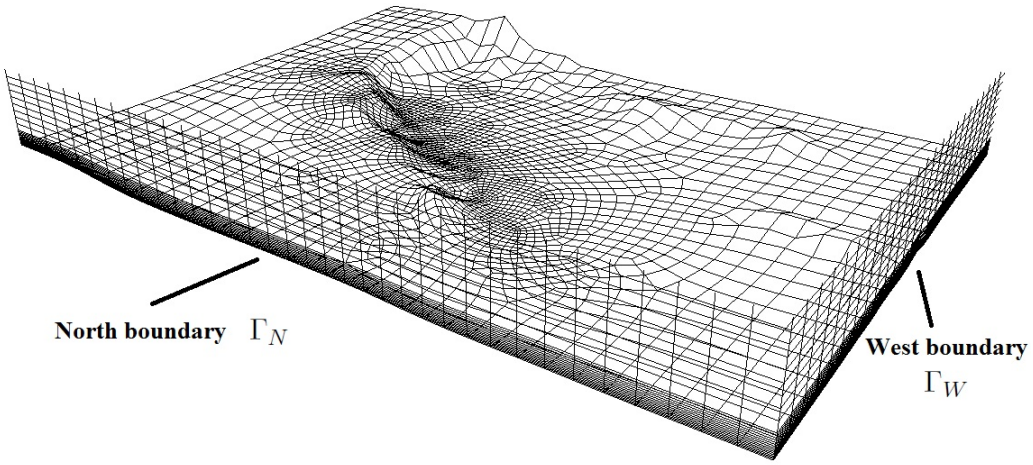

Figure 12: The lower surface, west boundary and the north boundary of the extruded mesh

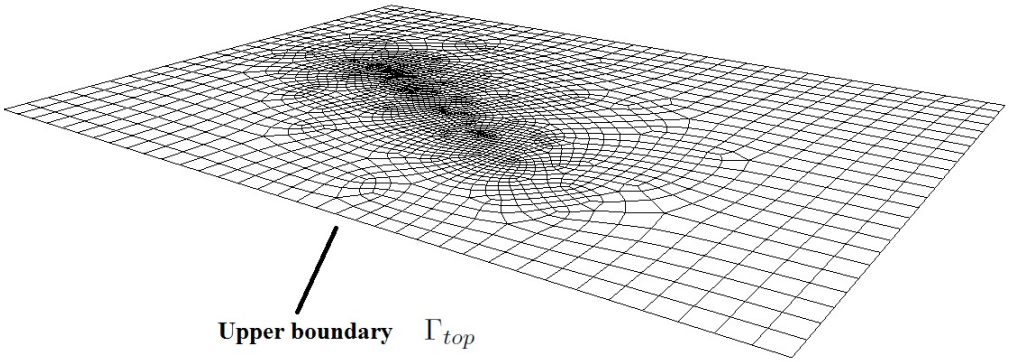

Figure 13: The upper surface of the extruded mesh

These subboundaries are shown in Figures 14 to 15.

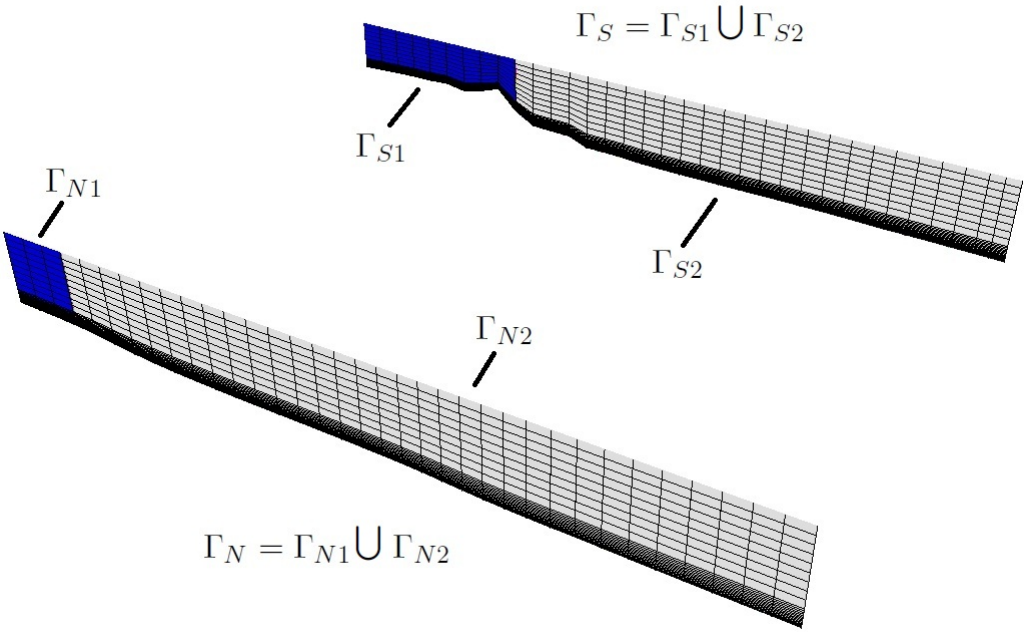

Figure 14: The divided west and north boundary of the extruded mesh

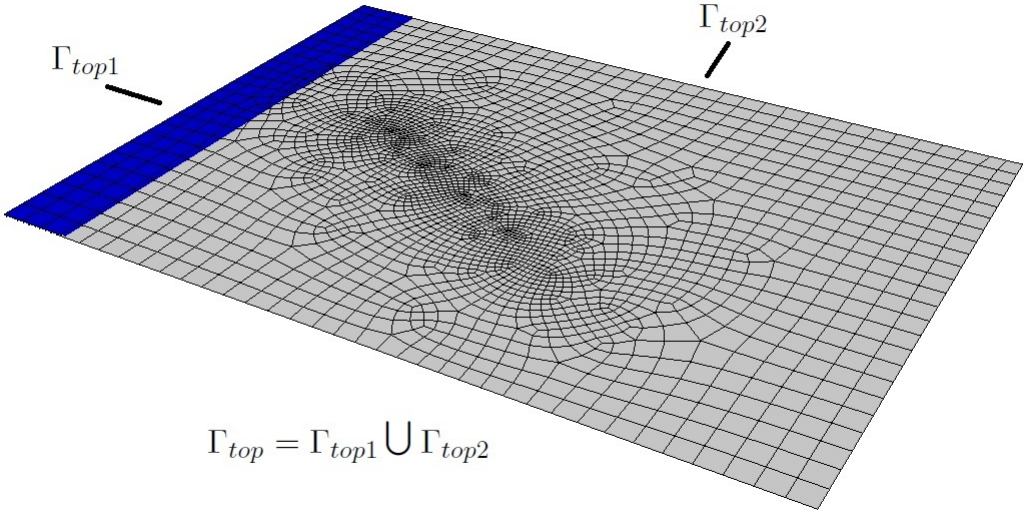

Figure 15: The divided upper surface of the extruded mesh

5 Model setup

5.1 Simulation with a katabatic flow profile

In order to avoid numerical instabilities we chose to first solve the wind field of the model domain, by using an inflow that matched the east component of the more easterly wind field (from the ECWMF re-analysis data), which was the mean direction plus the standard deviation for the direction, see Table 1 (in Section 6) and Figure 16 for the definition of this wind field.

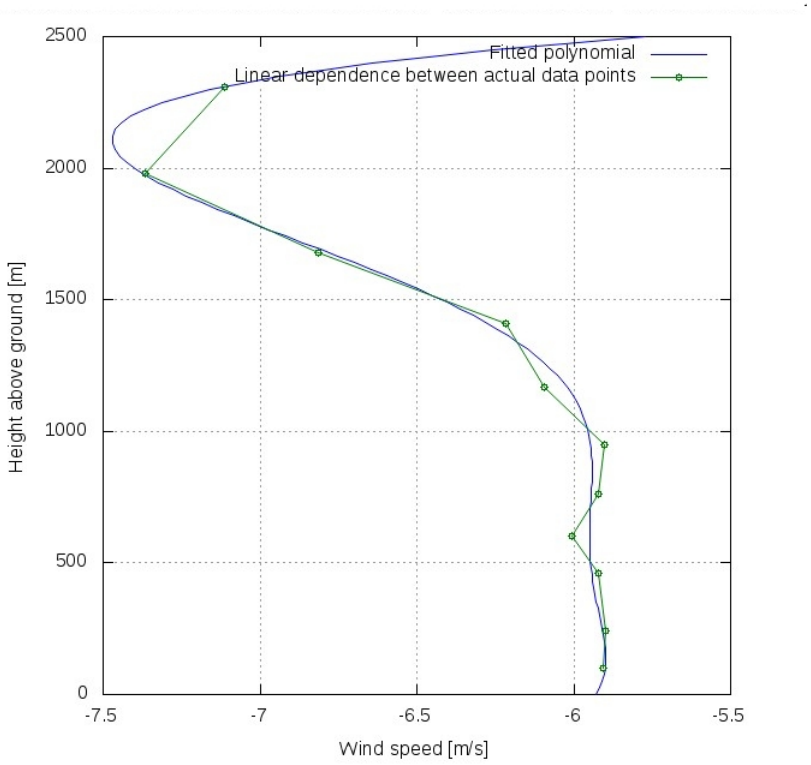

Figure 16: The inflow boundary condition profile, $E_{maxD}(h)$.

After solving the problem with this wind field we chose to include an inflow that described that of an katabatic jet blowing in towards the valley of SBB. In order to avoid a sudden impact to the flow, we used a linear time-ramp of 100 seconds for the katabatic profile to reach its maximum strength. The exact initial and boundary conditions are described in the following subsection.

5.2 The initial and boundary conditions for the first simulation

The initial condition for the model domain was chosen to be that of the inflow condition, therefore a sudden impact in the flow and numerical instabilities were avoided. The profile used for describing the initial and inflow conditions was

$$\begin{aligned} E_{maxD}(h) \;\approx\; & -5.929 \\ & +5.384 \times 10^{-4} \cdot h \\ & -2.870 \times 10^{-6} \cdot h^2 \\ & +4.968 \times 10^{-9} \cdot h^3 \\ & -3.394 \times 10^{-12} \cdot h^4 \\ & +7.343 \times 10^{-16} \cdot h^5, \end{aligned}$$

where h is the height above ground. The profile of the inflow was created from the ECMWF wind data. The regression analysis of the data is explained in detail in Section 6.

The initial condition for the first simulation was

$$u_1 = E_{maxD}(h) \text{ and } u_2, u_3 = 0 \qquad \text{in } \Omega \text{ for } t = 0,$$

where the notation u_1 refers to the velocity component in the local x-direction (west to east), notations u_2 and u_3 refer to the local $y-$ (south to north) and $z-$ directions.

The boundary conditions where

$$\begin{aligned} \vec{u} \cdot \vec{n} \,|_{\Gamma_E} &= E_{maxD}(h) \text{ and } u_2, u_3 \,|_{\Gamma_E} = 0 \\ \vec{u} \cdot \vec{n} \,|_{\Gamma_{top2} \bigcup \Gamma_{N2} \bigcup \Gamma_{S2}} &= 0 \text{ and } (\overline{\overline{\sigma}}\vec{n} - ((\overline{\overline{\sigma}}\vec{n}) \cdot \vec{n})\vec{n}) \,|_{\Gamma_{top2} \bigcup \Gamma_{N2} \bigcup \Gamma_{S2}} = \vec{0} \\ \vec{u} \,|_{\Gamma_{bed} \bigcup \Gamma_{top1} \bigcup \Gamma_{N1} \bigcup \Gamma_{S1}} &= \vec{0} \\ \bar{\bar{\sigma}}\vec{n} \,|_{\Gamma_W} &= \vec{0}. \end{aligned}$$

The time-step $\Delta t = 0.1$ s was used for a time-span of 700 seconds.

5.3 The initial and boundary conditions for the restart of the first simulation

After running the first simulation for 700 seconds (where the inflow had past the valley, where the BIAs exist), the simulation was restarted using an new inflow profile with a linear 100 second time-ramp of the katabatic wind profile combined with the earlier inflow profile at the east boundary. The profile of the katabatic wind was described by a second degree polynomial with a max velocity of 30 m/s and a height of 100 m. The function used for describing the katabatic velocity profile was

$$\begin{aligned} K(h) &\approx -1.776 \times 10^{-15} \\ &\quad +1.200 \cdot h \\ &\quad -1.200 \times 10^{-2} \cdot h^2 \qquad \text{for } 0 \geq h \leq 100 \end{aligned}$$

$$K(h) = 0 \qquad \text{for } h > 100,$$

where h is the height above ground.

The initial condition used for this simulation, was the solution of the velocity field in the first simulation at 700 seconds from initialization $\vec{u}_S$, meaning that

$$\vec{u} = \vec{u}_S \qquad \text{in } \Omega \text{ for } t_2 = 0,$$

where $t_2 = 0$ is equivalent to $t = 700$ s.

The boundary conditions for the restart simulation where

$$\begin{aligned} \vec{u} \cdot \vec{n} \,|_{\Gamma_E} &= -1 \cdot (E_{maxD}(h) + K(h) \cdot t_2/100) \text{ and } u_2, u_3 \,|_{\Gamma_E} = 0 \qquad \text{for } t_2 < 100\text{sec} \\ \vec{u} \cdot \vec{n} \,|_{\Gamma_E} &= -1 \cdot (E_{maxD}(h) + K(h)) \text{ and } u_2, u_3 \,|_{\Gamma_E} = 0 \qquad \text{for } t_2 \geq 100\text{sec} \end{aligned}$$

$$\vec{u} \cdot \vec{n} \,|_{\Gamma_{N2} \bigcup \Gamma_{S2}} = 0 \text{ and } (\overline{\overline{\sigma}}\vec{n} - ((\overline{\overline{\sigma}}\vec{n}) \cdot \vec{n})\vec{n}) \,|_{\Gamma_{N2} \bigcup \Gamma_{S2}} = \vec{0}$$

$$\vec{u} \,|_{\Gamma_{bed} \bigcup \Gamma_{N1} \bigcup \Gamma_{S1}} = \vec{0}$$

$$\bar{\bar{\sigma}}\vec{n} \,|_{\Gamma_W} = \vec{0}$$

$$\vec{u} \,|_{\Gamma_{top1} \bigcup \Gamma_{top2}} = \vec{u}_S(z) \text{ where } z = 2500\text{m},$$

where $\vec{u}_S$ stands for the solution of the earlier run at $t = 700$ s. This may be considered an artificial way of forcing the flow to stay inside the model domain. But we believe that this choice of boundary condition at the upper surface would not have any significant impact on the flow in the valley, since the profile of the katabatic wind, only extended 100m above ground. The time-step $\Delta t = 0.1$ s was used for a time-span of 1000 seconds.

6 Wind data

The wind patterns in Antarctica are mainly caused by a global pattern of atmospheric circulation. Because of the shape of Antarctica the circulation of air becomes relatively uniform, which complicates the weather patterns. Therefore Antarctica has a number of so called weather "bands", which all have individual weather conditions (Antarctic Connection, 2011).

The katabatic winds originate from temperature differences which means that differences in air density and pressure occur, these winds move from areas of higher pressure to areas of lower pressure. The colder air naturally has a higher pressure, therefore the dense air higher up will flow fast towards the surface. The katabatic winds at the coast of Antarctica may reach velocities of around 90 m/s (Antarctic Connection, 2011).

6.1 Wind data of SBB

The boundary conditions and velocity profiles for the SBB model were created by extracting reanalysis data from the ERA-Interim archive, ECMWF (Berrisford *et al.* , 2009). The extracts from the ERA files were provided by Sami Saarinen, application specialist at CSC, the Finnish IT Center for Science Ltd. As the ERA-Interim data does not take katabatic Winds into account, assumptions on the katabatic wind profiles had to be made from literature (Antarctic Connection, 2011).

The data was retrieved for 45 horizontal data locations in the surroundings of Scharffenberbotnen, with lat long coordinates from -74.00 to -75.00 latitude and 348.00 to 350.00 longitude, with a horizontal resolution of 0.25 degrees in both directions. The relations between the horizontal data points and the SBB model are presented in Figure 6, Section 1. The vertical data column of the node on the north east side of the model domain was used for creating the initial and boundary conditions. The decision to use only one data column will be justified later in this Section*.

Each vertical column of the ERA-Interim data consisted of 11 levels, these levels were expressed in pressure levels with units (hPa) and were then converted into meters above ground to act as input for our model. The conversion was done according to the ERA-Interm Archive (Berrisford *et al.* , 2009). The levels in meters where: 2310 m, 1980 m, 1680 m, 1410 m, 1170 m, 950 m, 760 m, 600 m, 460 m, 240 m and 100 m, hence the resolution was not uniform for the vertical data points.

The reanalysis data was extracted for every 15th day of each month in the year 2009 and at 4 different times for each of these days, leading to a daily resolution of

6 hrs. After plotting the directions and the magnitudes for each month, time and elevation for the four points closest to the SBB model, we could clearly see that the main wind directions were between north and east. These directions remained steady up to an elevation of 1500 meters above ground, and in order to create suitable inflow boundary conditions for the east and north border of our model, we decided to use the wind data from the data column north east of the model domain*.

The mean value for the wind directions and wind speeds were computed by creating a simple Matlab script to extract and evaluate the data. The mean wind speed is

$$\overline{s}(h) = \frac{\sum_{i=0}^{m} s_i(h)}{m}, \tag{53}$$

where $s_i(h)$ denotes the specific speed at a specific time i and a specific height h (meaning that the mean wind speed was calculated separately for each height), and m is the number of time levels, so $i = 1, 2, 3, ..., m$.

The mean direction was calculated in the same way, except that the speed component related to that direction and height was used as a weight factor for the directions, thus making the equation for the mean direction

$$\overline{d}(h) = \frac{\sum d_i(h) \cdot s_i(h)}{\sum s_i(h)}, \tag{54}$$

where $d_i(h)$ is the direction at a specific time and height.

The standard deviation of the sample, for the speed and direction at specific heights were calculated by

$$S = \sqrt{\frac{\sum (\overline{a}(h)) - a_i(h))^2}{m}}, \tag{55}$$

where a is denotes the sample value.

The velocity components in the north and east directions were calculated by multiplying the speed and direction components, thus the north components N_h were derived by $N_h = \overline{s_h} \cdot \cos \overline{d_h}$, where the subscript h means that this is done for each height separately. From this of course follows that the east component was calculated by $E_h = \overline{s_h} \cdot \sin \overline{d_h}$. The direction d at elevation h describes the angle (in radians) of the wind from the east direction rotating counterclockwise, see Figure 17. The north and east components with the deviations in direction are calculated by $N_h = \overline{s_h} \cdot \cos \overline{d_h} \pm S_d$ and $E_h = \overline{s_h} \cdot \sin \overline{d_h} \pm S_d$, where S_d is the standard deviation of the direction at the height h.

The directions at different heights describe the direction that the wind is blowing

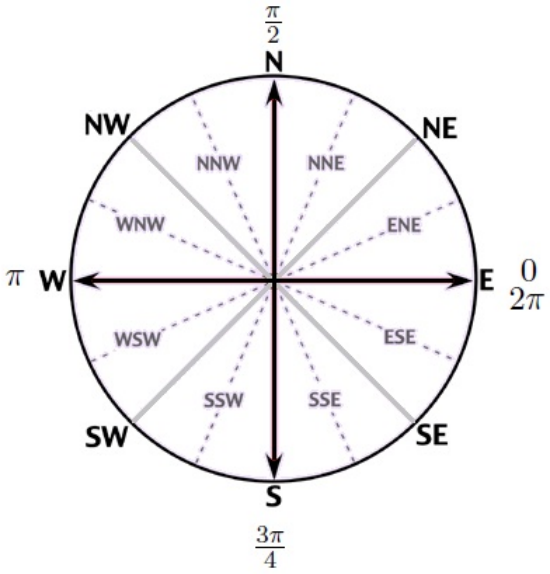

Figure 17: The definition of the direction, shown in radians

Table 1: Mean values for wind speed and wind direction at different heights above ground

height [m]	Direction [rad]	Speed [m/s]	SD Direction [rad]	SD Speed [m/s]
2310	-2.4676	7.8546	1.3347	7.4005
1980	-2.3940	7.4804	0.64699	6.8055
1680	-2.1902	6.9478	0.42193	4.9980
1410	-1.9916	6.4681	0.70075	4.4356
1170	-1.9101	6.4544	0.67435	3.6588
950	-1.8294	6.4063	0.65819	3.7553
760	-1.8468	6.3927	0.66289	3.8004
600	-1.8500	6.4547	0.65429	3.9671
460	-1.8655	6.3809	0.67597	3.8554
240	-1.8633	6.3868	0.68579	3.8674
100	-1.8547	6.3769	0.67104	3.8516

in at that specific height, meaning that a value of about -1.85 radians is a wind blowing approximately from the north east, these values are presented in Table 1.

6.2 Regression analysis of the SBB wind data

In order to create suitable boundary conditions the wind profiles were approximated to suite the model by fitting polynomials to the data points. This was done by using the method of least squares, which minimizes the distance between the data points and the polynomial.

The purpose of a regression analysis was to create a polynomial $y(x)$ of nth degree to fit a set of p pairs of data points $(x_1, y_1), (x_2, y_2), (x_3, x_4), ..., (x_p, y_p)$, where $p > n$.

The differences between the original data and the approximated polynomial is called the residual, and the method of least squares states that the polynomial best suited to describe a set of data points, is the one for which the sum of the squares of the residuals is the smallest.

The square of the residual for the data points of a nth degree polynomial is

$$r_k^2 = (y_k - a_0 - a_1 x_k - a_2 x_k^2 ... - a_n x_k^n)^2. \tag{56}$$

Respectively the sum of the squares of the residuals for any polynomial of nth degree is then

$$S = \sum_{k=1}^{m} (y_k - a_0 - a_1 x_k - a_2 x_k^2 ... - a_n x_k^n)^2 = r^2. \tag{57}$$

In order to minimize the equation (57) one has to set the gradient to be zero, which leads to the following equation

$$\frac{\partial S}{\partial a_j} = 0, \qquad \text{where } j \in [0, n]. \tag{58}$$

One way to solve the problem is to put the system in a matrix form

$$\begin{pmatrix} m & \sum x_k & \sum x_k^2 & ... & \sum x_k^n \\ \sum x_k & \sum x_k^2 & \sum x_k^3 & ... & \sum x_k^{n+1} \\ \sum x_k^2 & \sum x_k^3 & \sum x_k^4 & ... & \sum x_k^{n+2} \\ \vdots & \vdots & \vdots & \vdots & \vdots \\ \sum x_k^n & \sum x_k^{n+1} & \sum x_k^{n+2} & ... & \sum x_k^2 n \end{pmatrix} \begin{pmatrix} a_0 \\ a_1 \\ a_2 \\ \vdots \\ a_n \end{pmatrix} = \begin{pmatrix} \sum y_k \\ \sum x_k y_k \\ \sum x_k^2 y_k \\ \vdots \\ \sum x_k^n y_k \end{pmatrix}, \tag{59}$$

and then solve the column with the unknowns $(a_0, a_1, a_2, ..., a_n)$ by using the Gauss-Jordan elimination.

The approximated polynomials for the wind profiles are from 5th to 7th degree polynomials, depending on the suitability. The profiles are presented in Figures B.1 - B.6 in Appendix B.

7 Results

In this section we present the results of the simulation and discuss the effect they might have on the snow redistribution. The results for the simulation of an inflow condition of the katabatic profile with a 100 second time-ramp and a restart position of 700 seconds from initialization with an eastern inflow along with the other boundary conditions of the simulation are presented here. The simulation was run until 1000 seconds from initialization.

7.1 Results of the katabatic wind simulation

Orthographic projections of the simulation are presented in Figures 19 - 25, where the velocity vectors are plotted from the ground up to 15 m above ground. The length and the color of the vectors describe the absolute velocity, and the velocity direction is described by the direction of the vectors. The UTM29C coordinates are plotted on the axes and the color scale describes the absolute velocity of the vectors, which in the simulation results is cut off to 40 m/s, meaning that all velocities higher than 40 m/s are presented as 40 m/s. The blue ice areas are shown in the figure backgrounds as light gray areas, the exposed rocks on top of hills and mountains are located at the dark gray areas and the moraines are indicated with black areas. The borders present a rough outline of the area used in for our simulation domain.

There are clear re-circulation areas in the wake of the north east mountains (at approximately 436-437 km easting, 1724.5-1725.5 km northing, 437.5-438 km easting, 1724.5-1725.5 km northing and 438.5-439 km easting, 1723-1723.5 km northing) where snow is observed to be accumulated (Sinisalo *et al.* , 2004), see Figures 21-24. Higher velocities are found in the locations of the BIAs, especially as the katabatic front approaches these areas. From Figure 18 it is clear to see that the magnitude of the velocities above the BIAs is approximately only 7-10 m/s when the average wind acted as the inflow profile. Figures 19-24, where the impact of the katabatic inflow profile has reached the valley clearly indicate velocities of a much higher magnitude (locally above 30 m/s) at these areas, suggesting that the average wind speeds as such do not cause the snow to be ripped of the BIAs, but rather that the impact of the incoming katabatic wind can cause temporal high velocity zones at these areas.

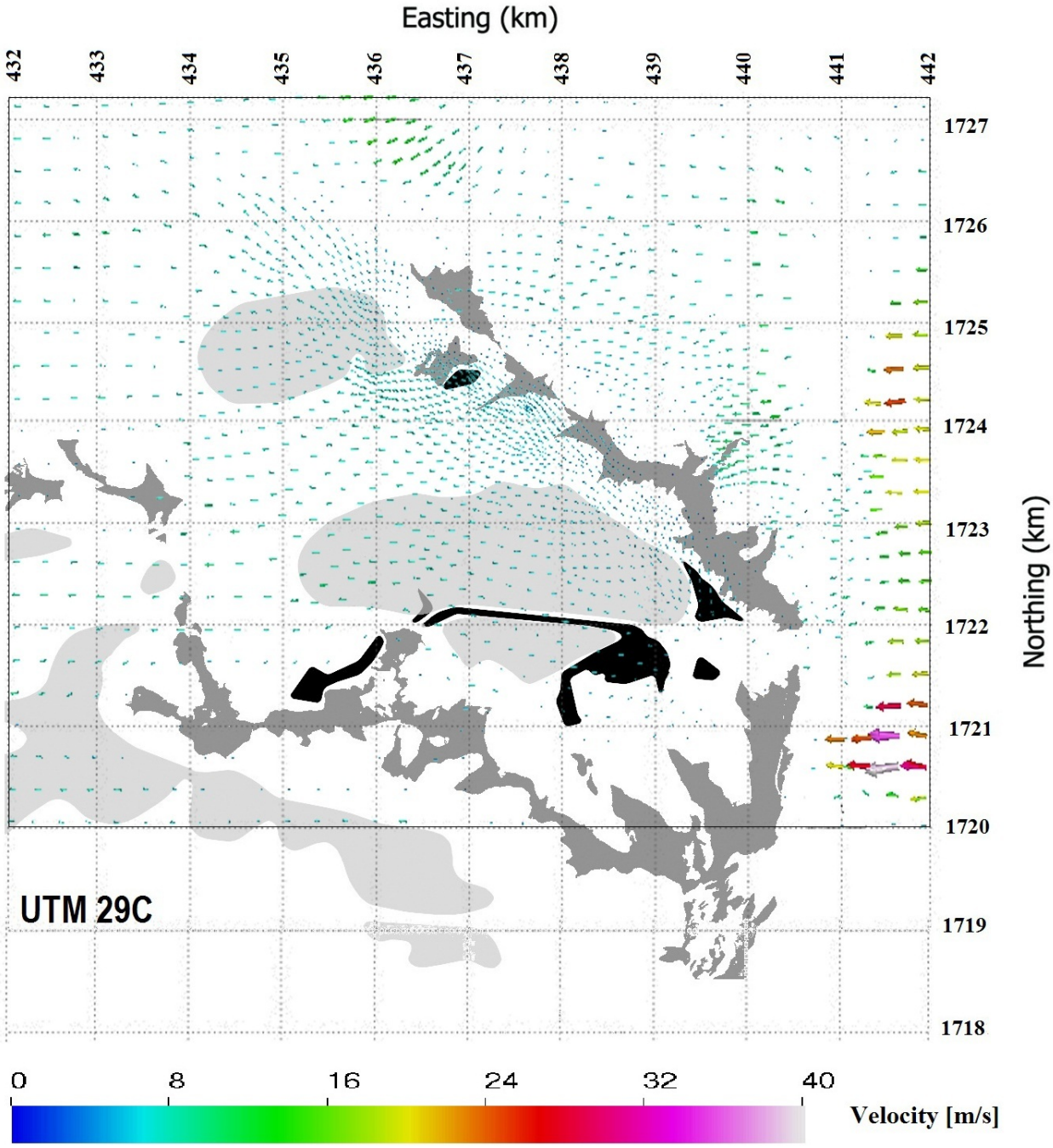

Figure 18: Results of the simulation with the average wind profile acting as an inflow condition. The solution is the flow field after 700 seconds from the start of the initial simulation with only the east wind profile acting as an inflow. The vectors are plotted from the ground up to 15 m above ground. The impact of the inflow has already reached the end of the valley. The magnitude of the velocities above the BIAs is approximately only 7-10 m/s.

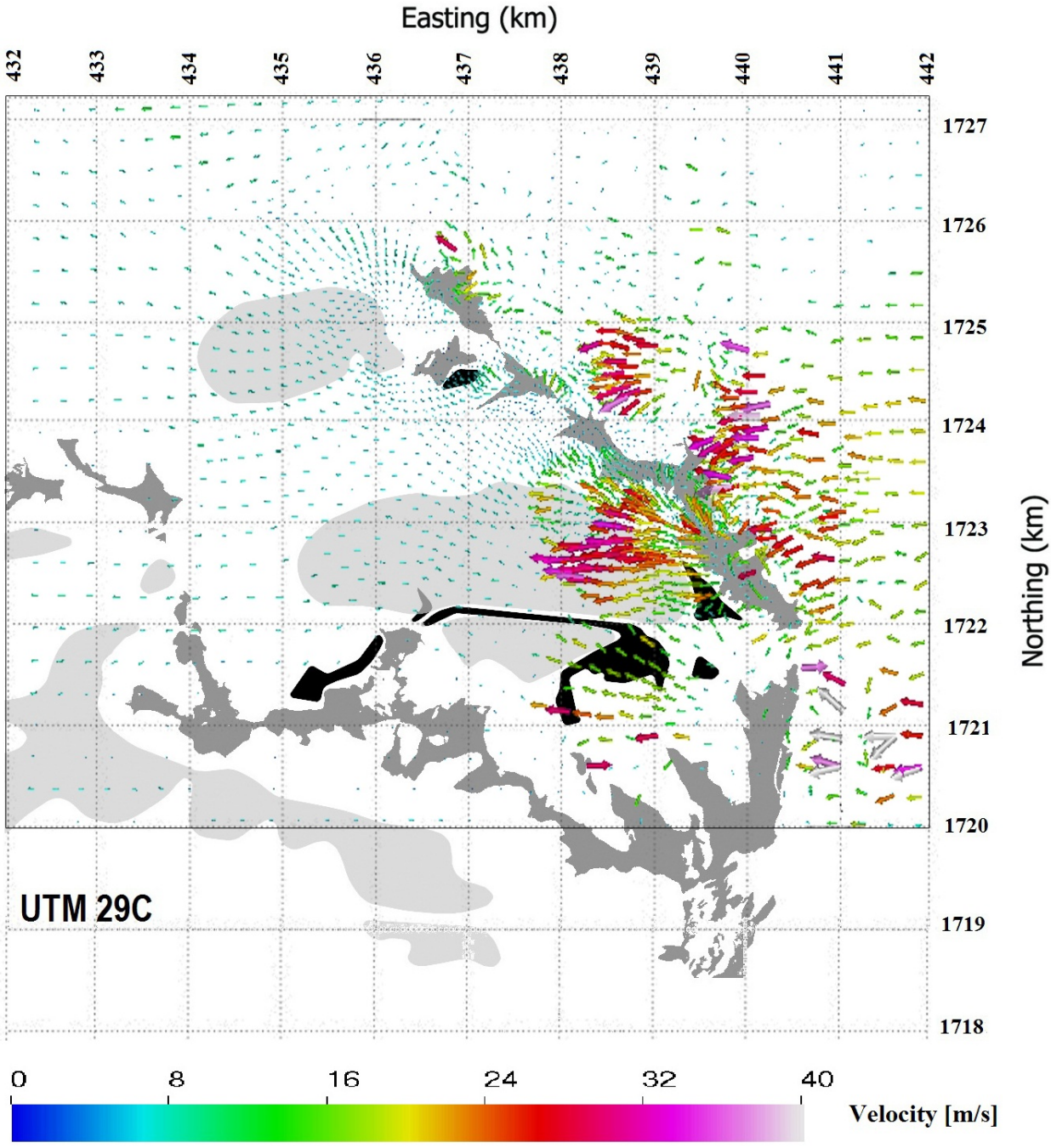

Figure 19: Results of the restart simulation with the katabatic profile acting as an inflow profile. The solution of the flow is presented at 400 seconds from initialization. The vectors are plotted from the ground up to 15 m above ground. The katabatic flow has just reached the valley and a clear impact can be seen at the eastern part of the larger BIA (located at approximately 435-439.5 km easting, 1722-1723.5 km northing) where the velocities reach up to approximately 35 m/s.

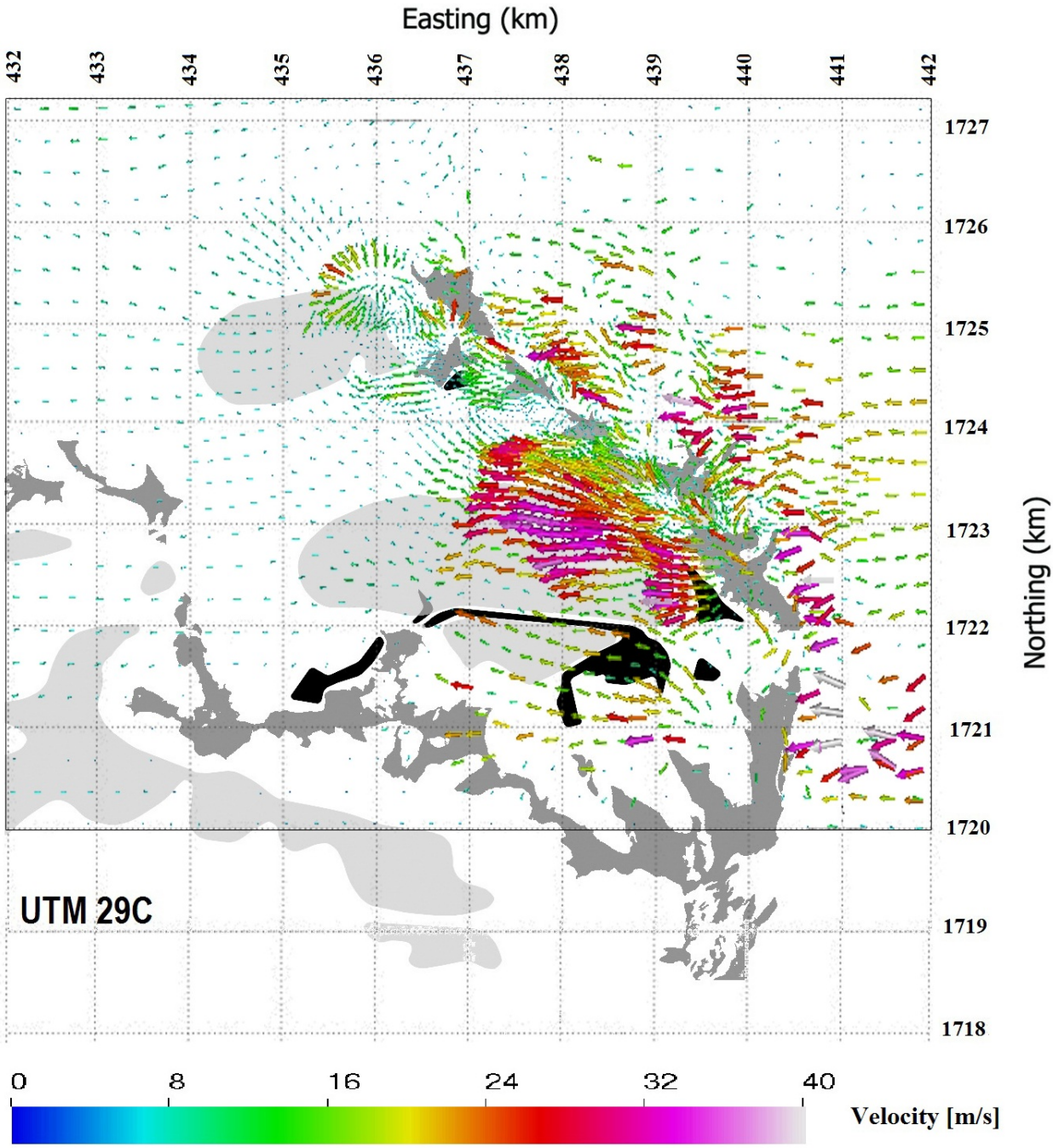

Figure 20: Results of the restart simulation with the katabatic profile acting as an inflow profile. The solution of the flow is presented at 500 seconds from initialization. The vectors are plotted from the ground up to 15 m above ground. The katabatic flow still has a clear impact at the eastern part of the larger BIA (located at approximately 435-439.5 km easting, 1722-1723.5 km northing) where the velocities reach up to approximately 35 m/s. Re-circulation areas in the wake of the north east mountains (locations at approximately 436-437 km easting, 1724.5-1725.5 km northing, 437.5-438 km easting, 1724.5-1725.5 km northing and 438.5-439 km easting, 1723-1723.5 km northing) where snow is observed to be accumulated are becoming more evident.

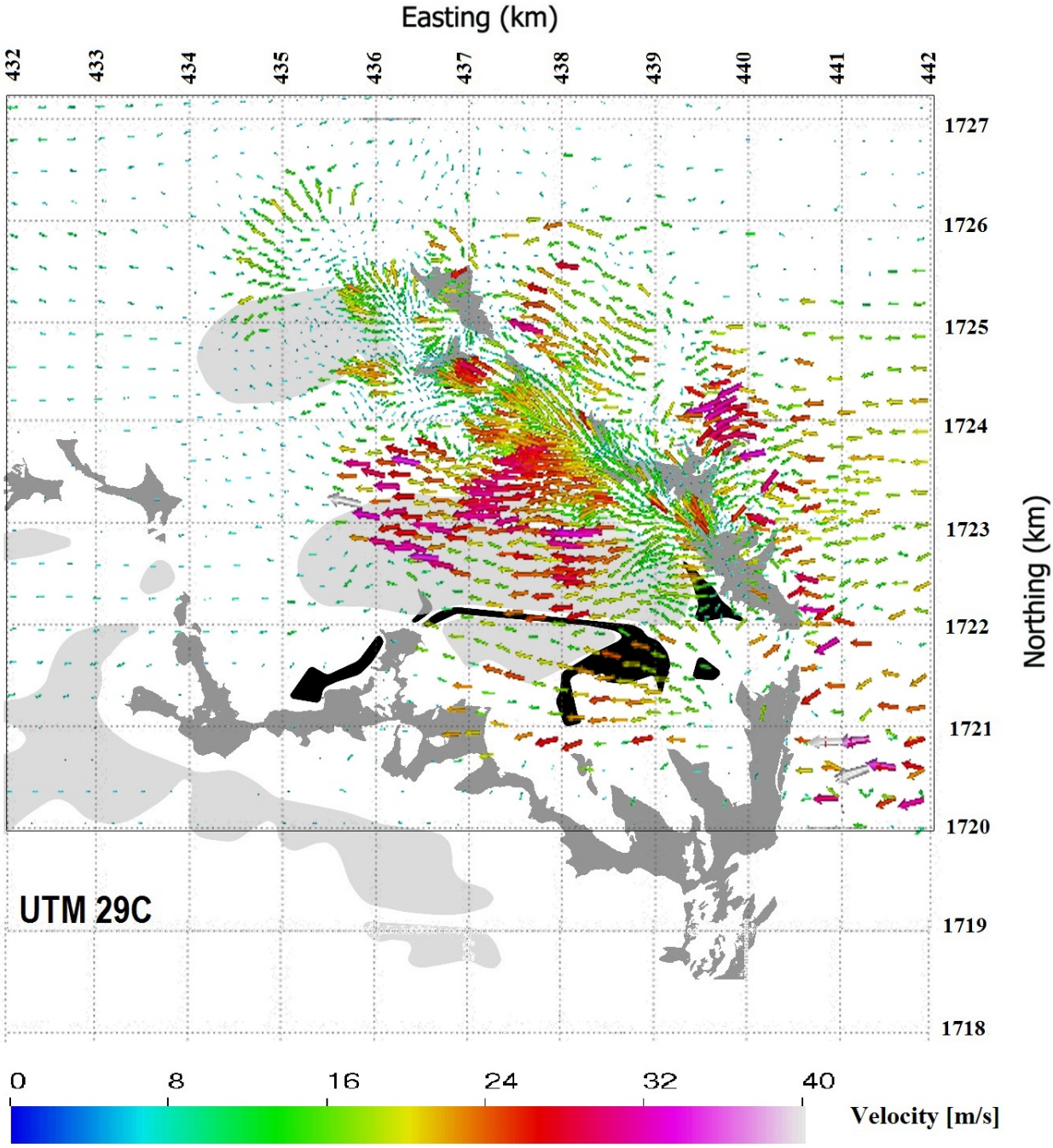

Figure 21: Results of the restart simulation with the katabatic profile acting as an inflow profile. The solution of the flow is presented at 600 seconds from initialization. The vectors are plotted from the ground up to 15 m above ground. High magnitude velocities (locally over 35 m/s) have stretched above most of the larger BIA (located at approximately 435-439.5 km easting, 1722-1723.5 km northing). Extreme recirculation areas are also apparent at the locations where snow has been observed to be accumulated (at approximately 436-437 km easting, 1724.5-1725.5 km northing, 437.5-438 km easting, 1724.5-1725.5 km northing and 438.5-439 km easting, 1723-1723.5 km northing)

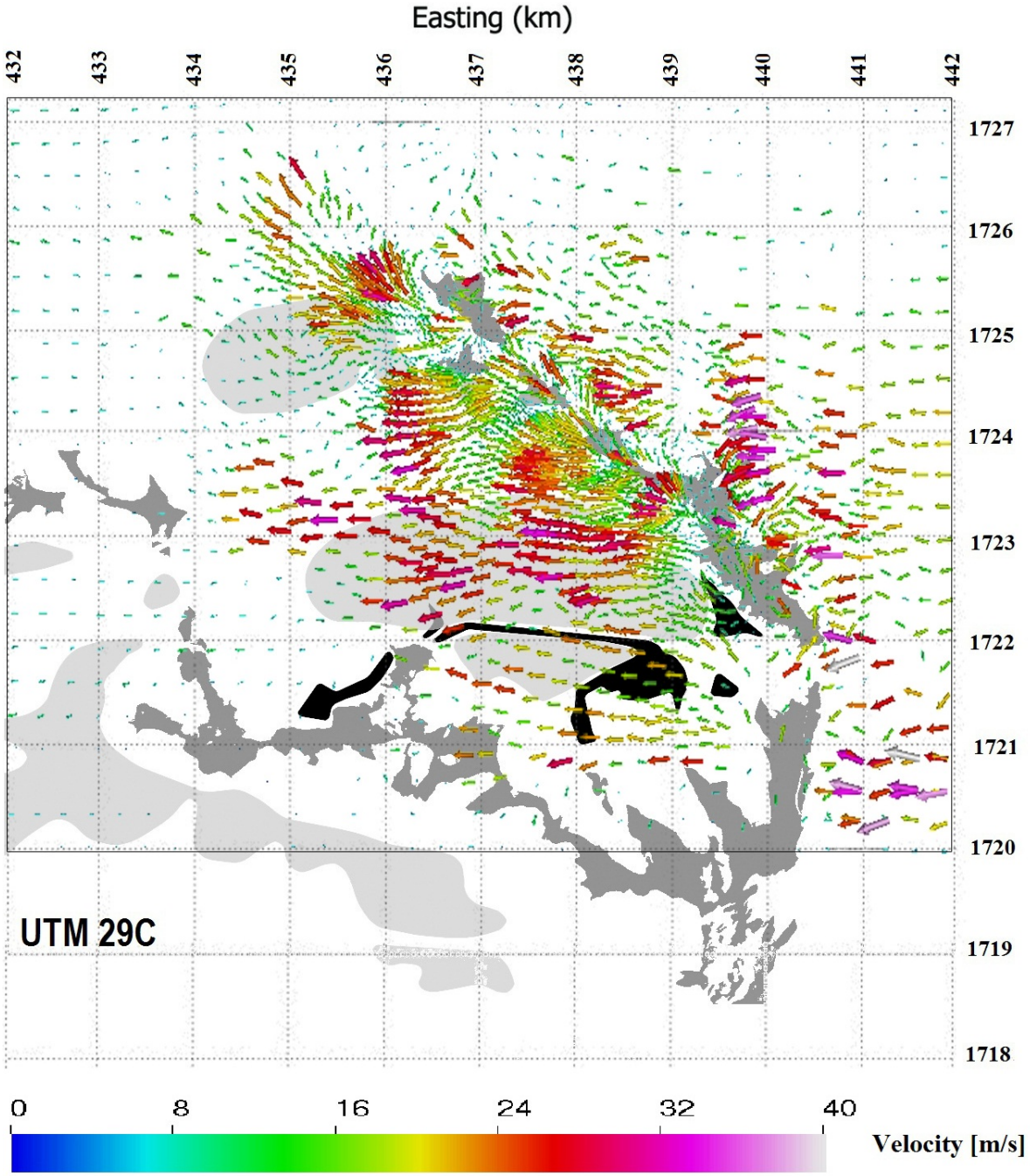

Figure 22: Results of the restart simulation with the katabatic profile acting as an inflow profile. The solution of the flow is presented at 700 seconds from initialization. The vectors are plotted from the ground up to 15 m above ground. Velocities of approximately 30-35 m/s are found above the entire larger BIA (located at approximately 435-439.5 km easting, 1722-1723.5 km northing). High magnitude velocities are also apparent at the north east border of the smaller BIA (located at approximately 434-436 km easting, 1724-1725.5 km northing).

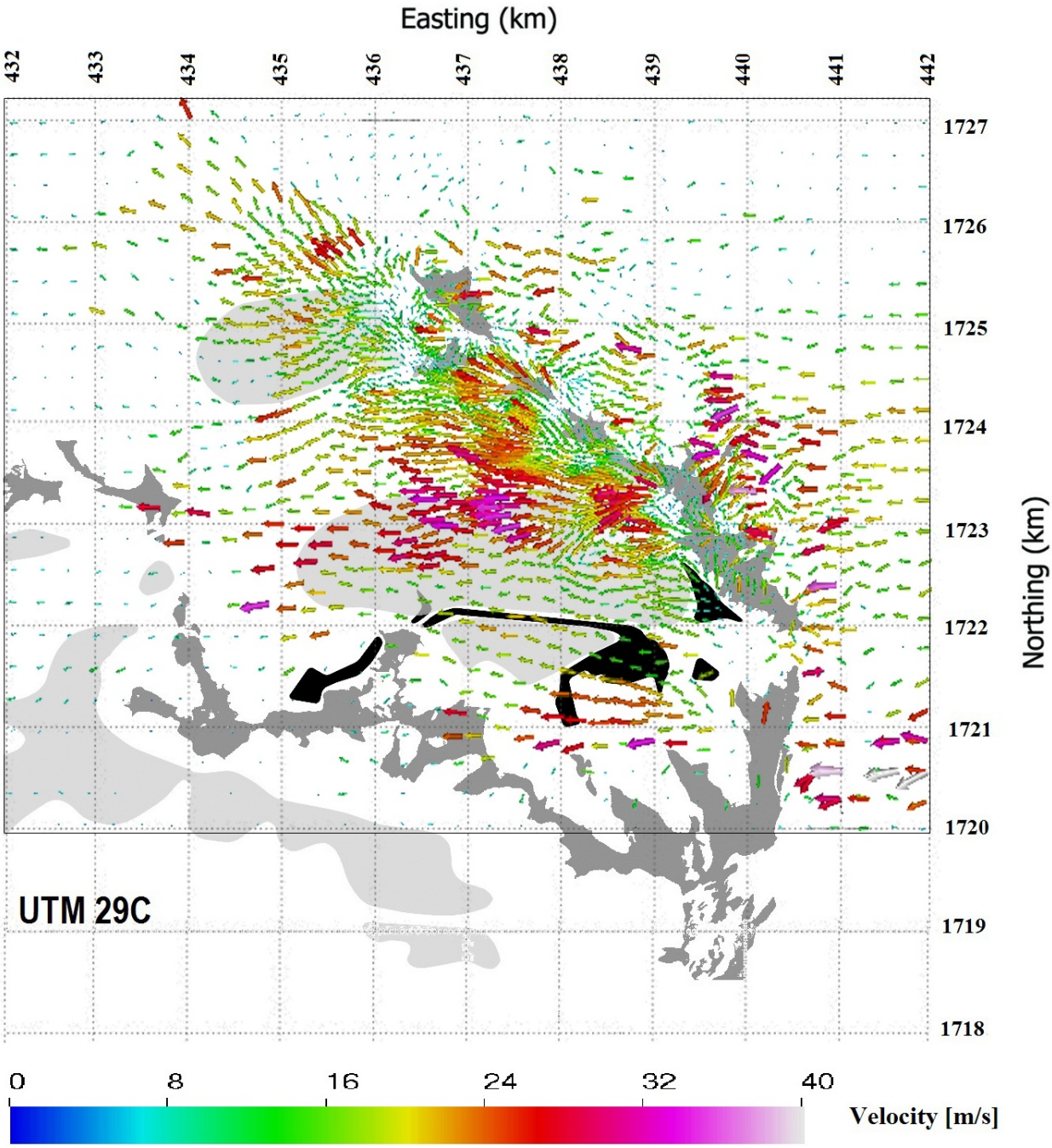

Figure 23: Results of the restart simulation with the katabatic profile acting as an inflow profile. The solution of the flow is presented at 800 seconds from initialization. The vectors are plotted from the ground up to 15 m above ground.

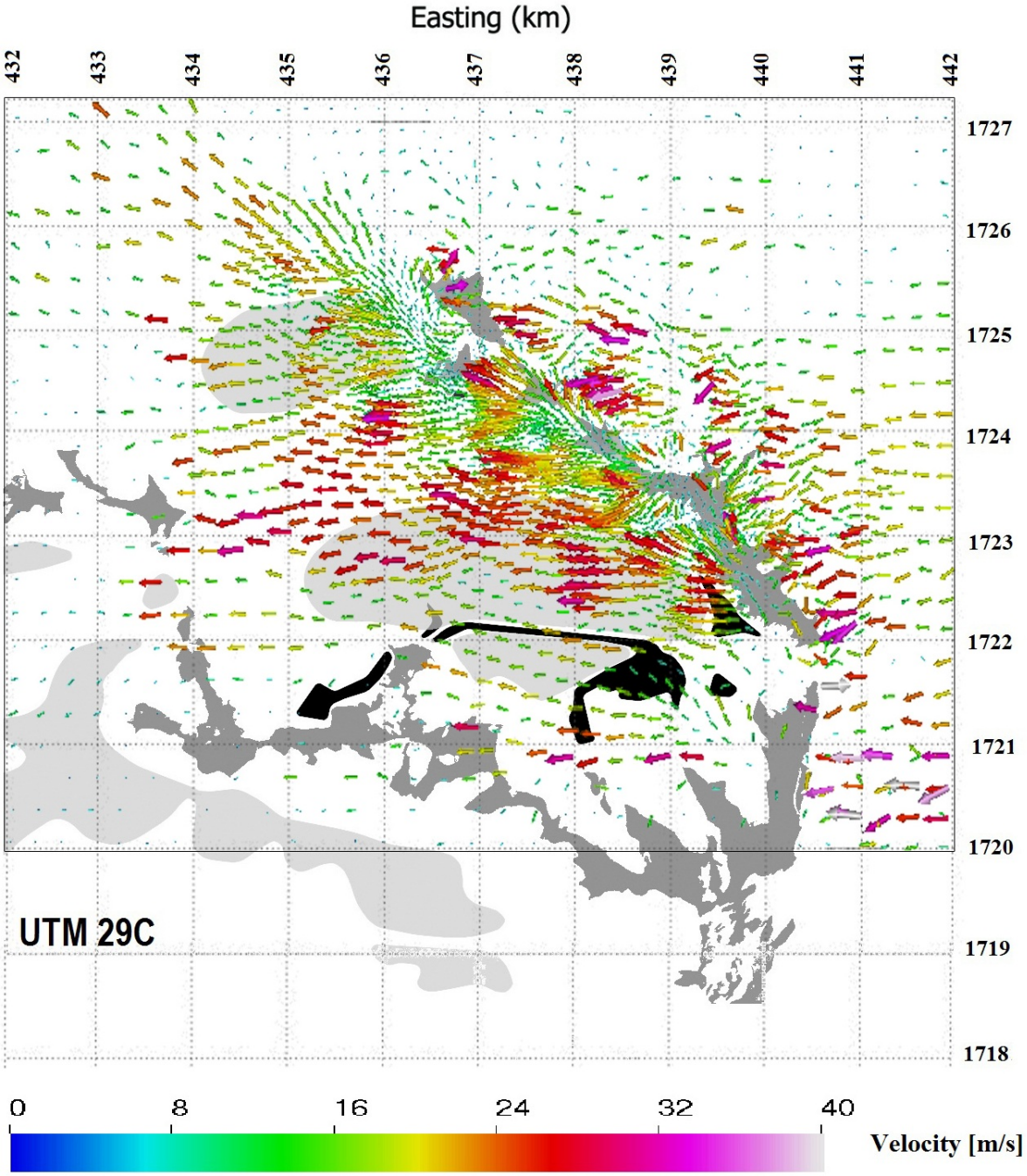

Figure 24: Results of the restart simulation with the katabatic profile acting as an inflow profile. The solution of the flow is presented at 900 seconds from initialization. The vectors are plotted from the ground up to 15 m above ground.

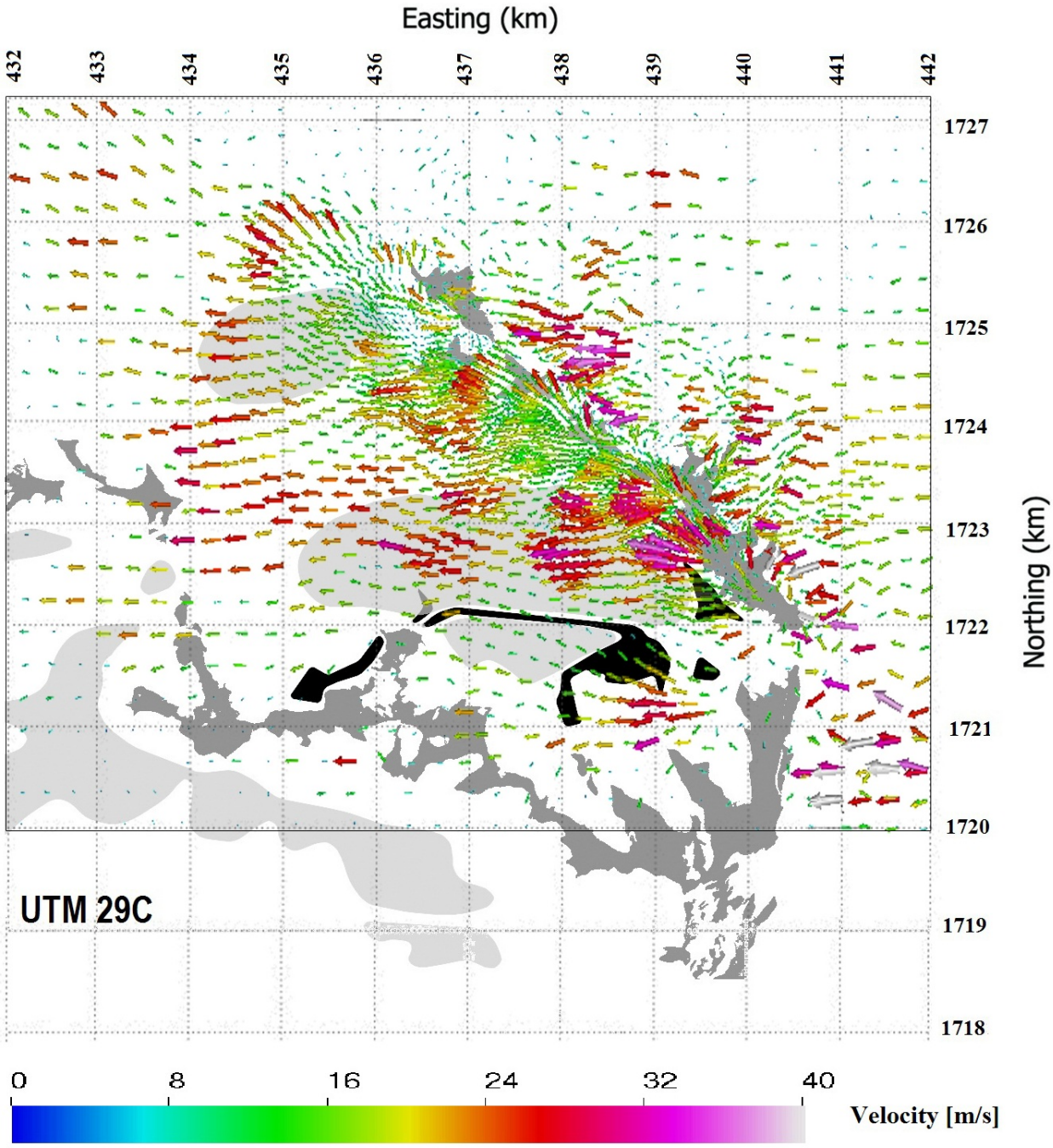

Figure 25: Results of the restart simulation with the katabatic profile acting as an inflow profile. The solution of the flow is presented at 1000 seconds from initialization. The vectors are plotted from the ground up to 15 m above ground.

The transfer of linear momentum in turbulent flow close to the valley surface happens at length scales, that are not resolved in our computational mesh. Their effect on the flow then has to be modeled, which in our particular application is achieved by the VMS method. In contrary to RANS, in VMS a turbulent viscosity is not directly accessible and consequently a direct derivation of turbulent shear stresses from the obtained velocity field is not possible. Instead, we use the Cauchy stress tensor (and hence the molecular viscosity) to compute a surface shear stress from the velocity field. This certainly is far from being a quantitative measure of the effective (turbulent) wall shear stresses, nevertheless, its relative distribution points out the location at the valley glacier, where enhanced surface stresses occur.

The shear stress at the surface is presented in Figures 26 - 32, with the location of the Blue Ice Areas denoted by the dotted outlining, the exposed rocks on top of hills and mountains are shown as a 45 degree dark gray pattern and the moraines are located inside of the black bordered areas.

A general striking coincidence of accelerated flow and increased shear stress above the larger BIA (at approximately 435-439.5 km easting, 1722-1723.5 km northing) in the valley is clearly visible especially in Figures 19-22 and 26 - 29. These values seem to peak as the katabatic front hits the valley, suggesting that the highest velocities and shear stresses above the BIAs are caused by the sudden impact of an incoming flow. The flow above the BIA in the northern part of the valley (at approximately 434-436 km easting, 1724-1725.5 km northing) does not seem to be prone to velocities of the same magnitude as the larger one. We believe that variations in the inflow direction would lead to greater velocities in this area.

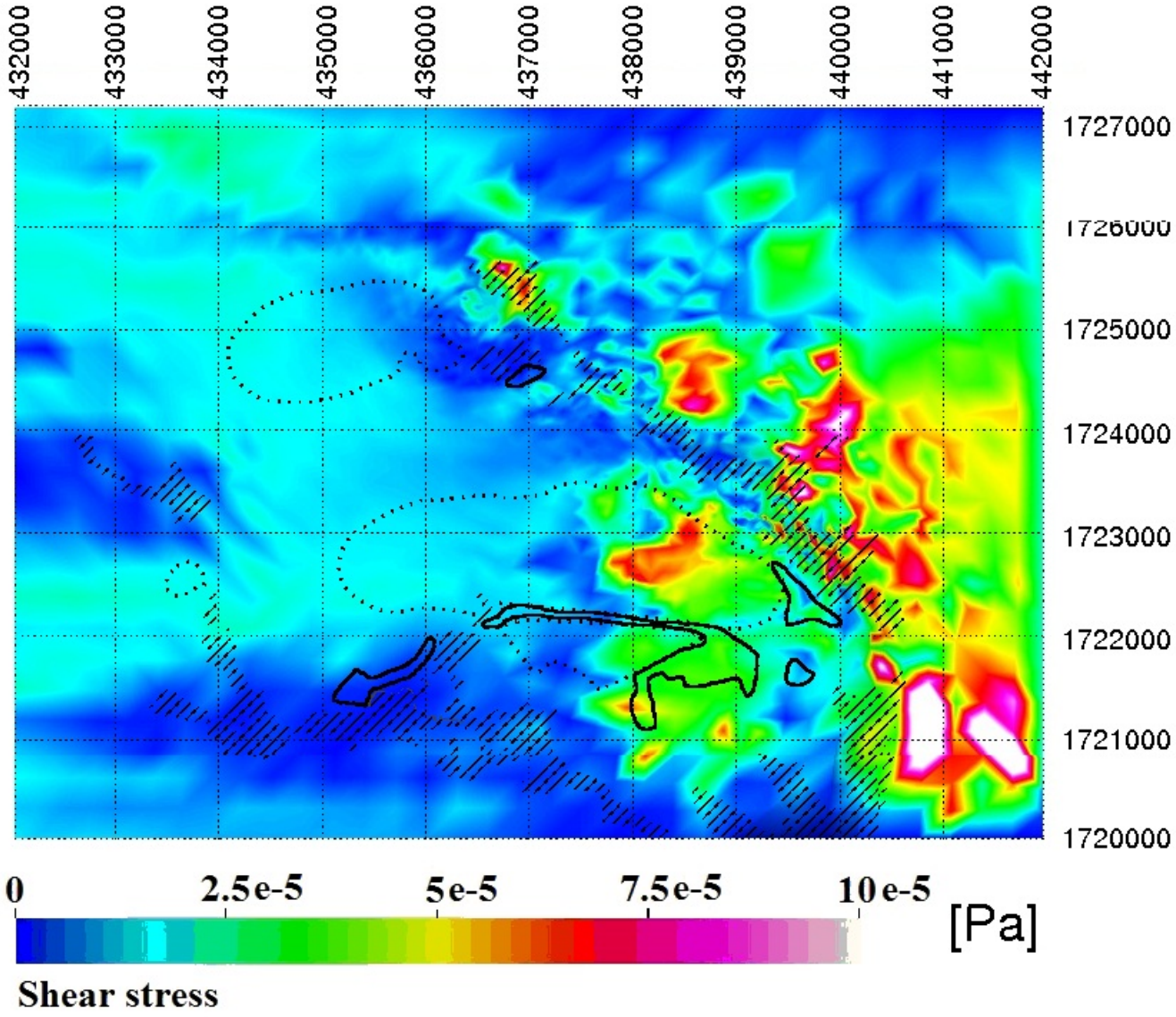

Figure 26: Results of the restart simulation with the katabatic profile acting as an inflow profile. This Figure indicates the absolute shear stress at 400 seconds from initialization. A clear increase in the absolute shear stress is evident at the eastern border of the larger BIA (located at approximately 435-439.5 km easting, 1722-1723.5 km northing). The impact of the katabatic wind profile is becoming evident as the flow has just reached the valley, compare to Figure 19 where the velocity field is shown at the same instant.

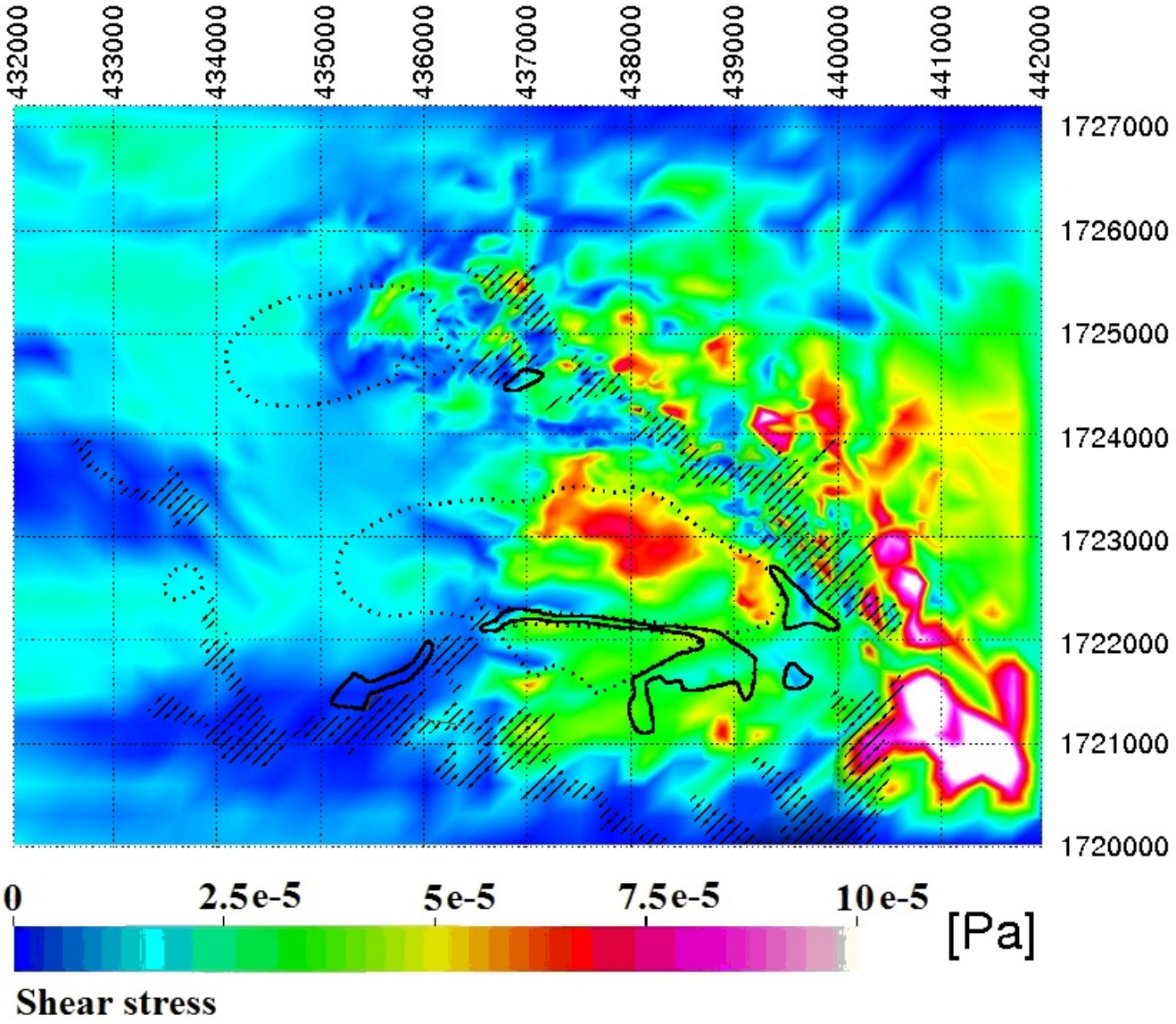

Figure 27: Results of the restart simulation with the katabatic profile acting as an inflow profile. This Figure indicates the absolute shear stress at 500 seconds from initialization. An absolute shear stress with a relatively higher magnitude than the other areas in the valley has stretched to cover a larger area (compared to the results at 400 s, see Figure 26) at the larger BIA (located at approximately 435-439.5 km easting, 1722-1723.5 km northing).

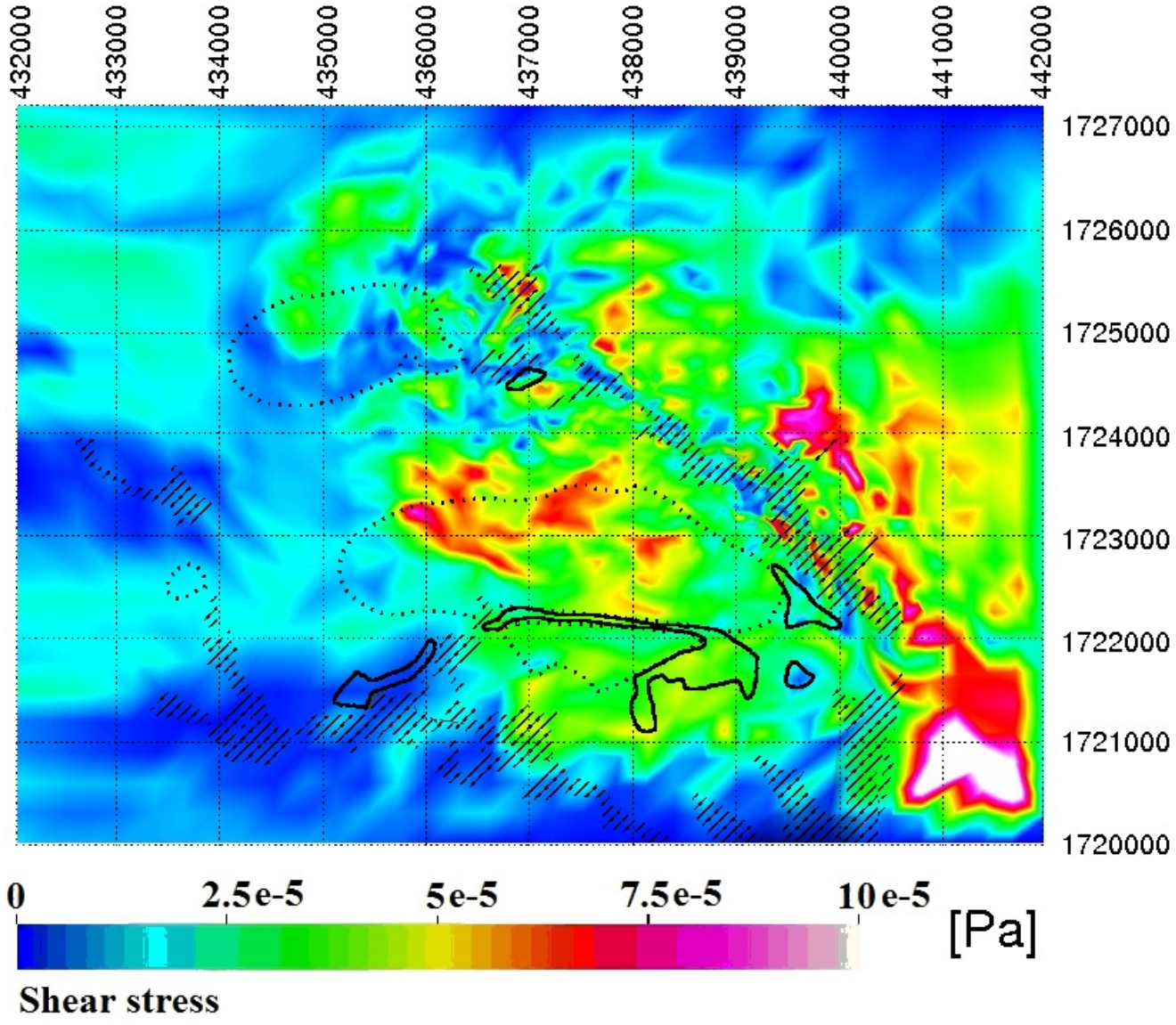

Figure 28: Results of the restart simulation with the katabatic profile acting as an inflow profile. This Figure indicates the absolute shear stress at 600 seconds from initialization.

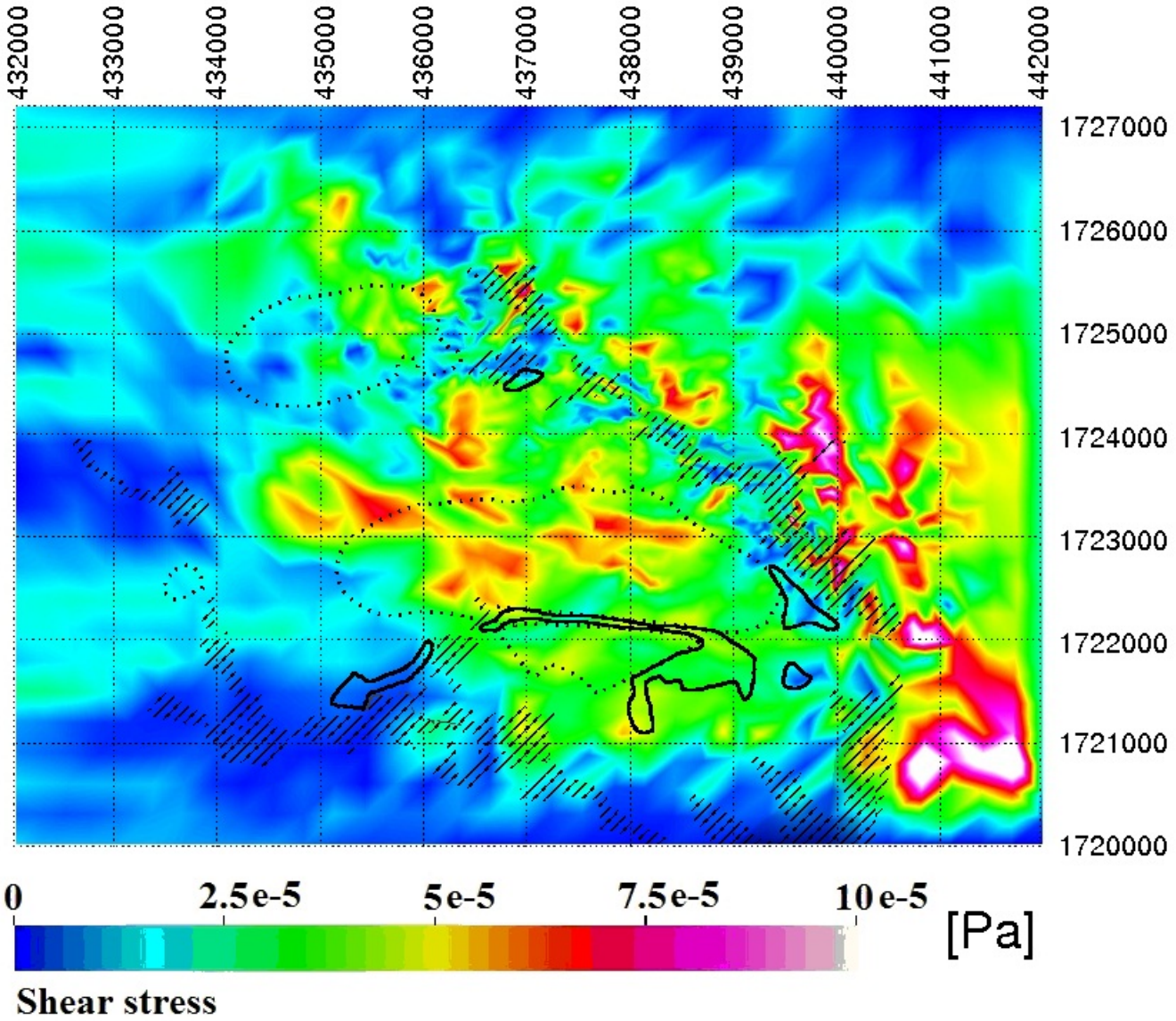

Figure 29: Results of the restart simulation with the katabatic profile acting as an inflow profile. This Figure indicates the absolute shear stress at 700 seconds from initialization. An increased shear stress is still evident in the larger part of the area covering the BIA located at approximately 435-439.5 km easting, 1722-1723.5 km northing.

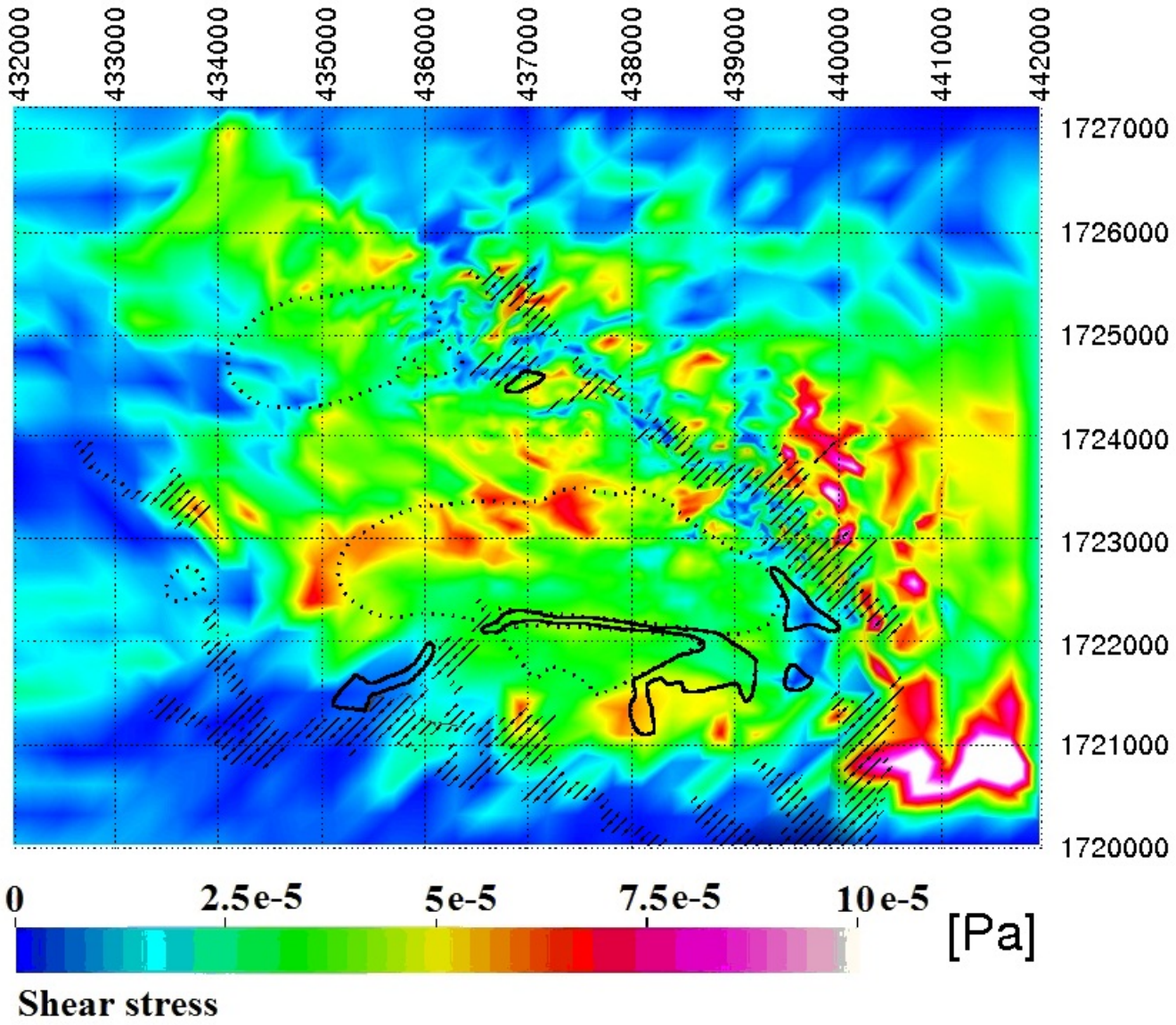

Figure 30: Results of the restart simulation with the katabatic profile acting as an inflow profile. This Figure indicates the absolute shear stress at 800 seconds from initialization. Increased values of the absolute shear stress can still be found on the northern border of the larger BIA (located at approximately 435-439.5 km easting, 1722-1723.5 km northing).

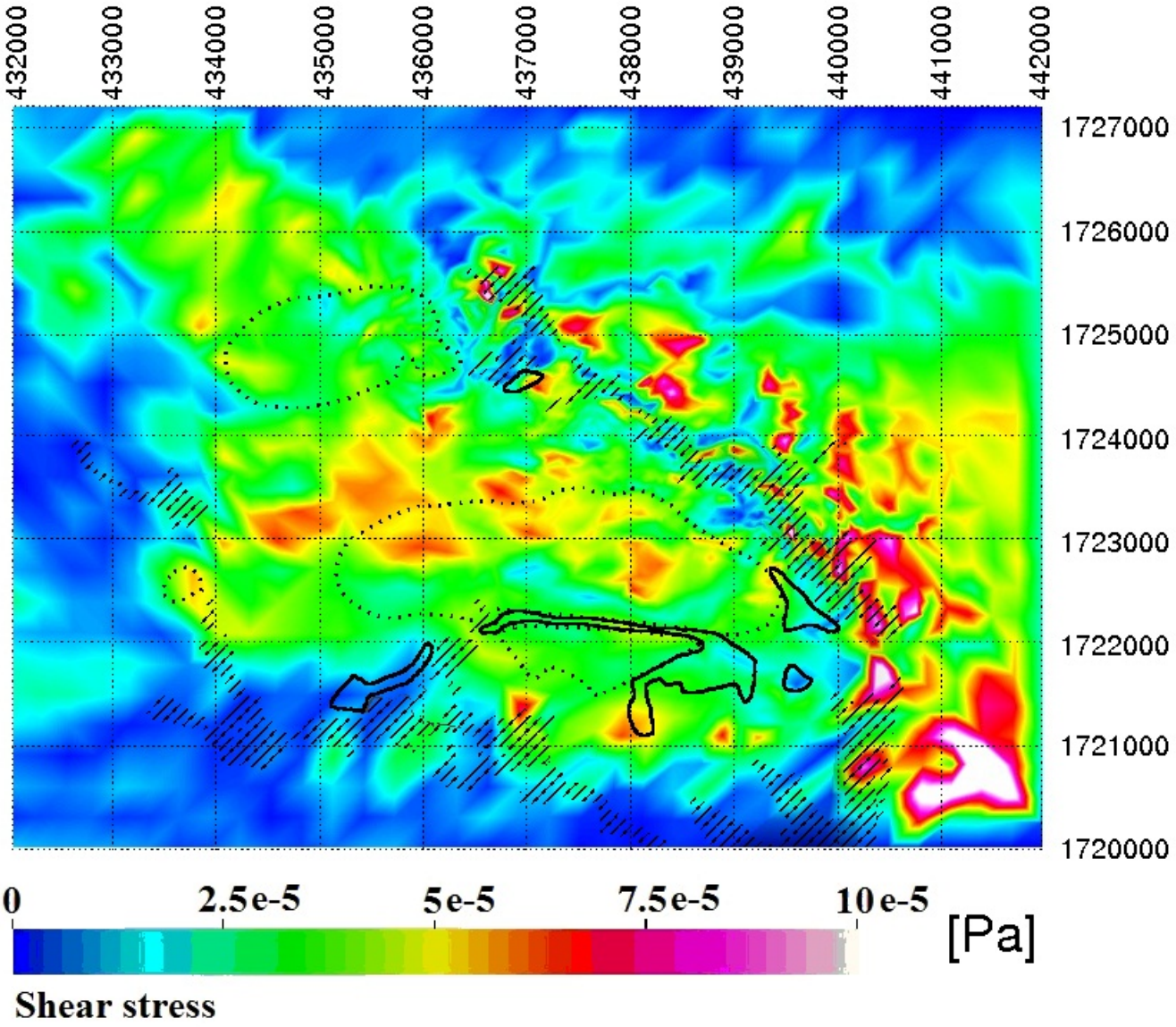

Figure 31: Results of the restart simulation with the katabatic profile acting as an inflow profile. This Figure indicates the absolute shear stress at 900 seconds from initialization.

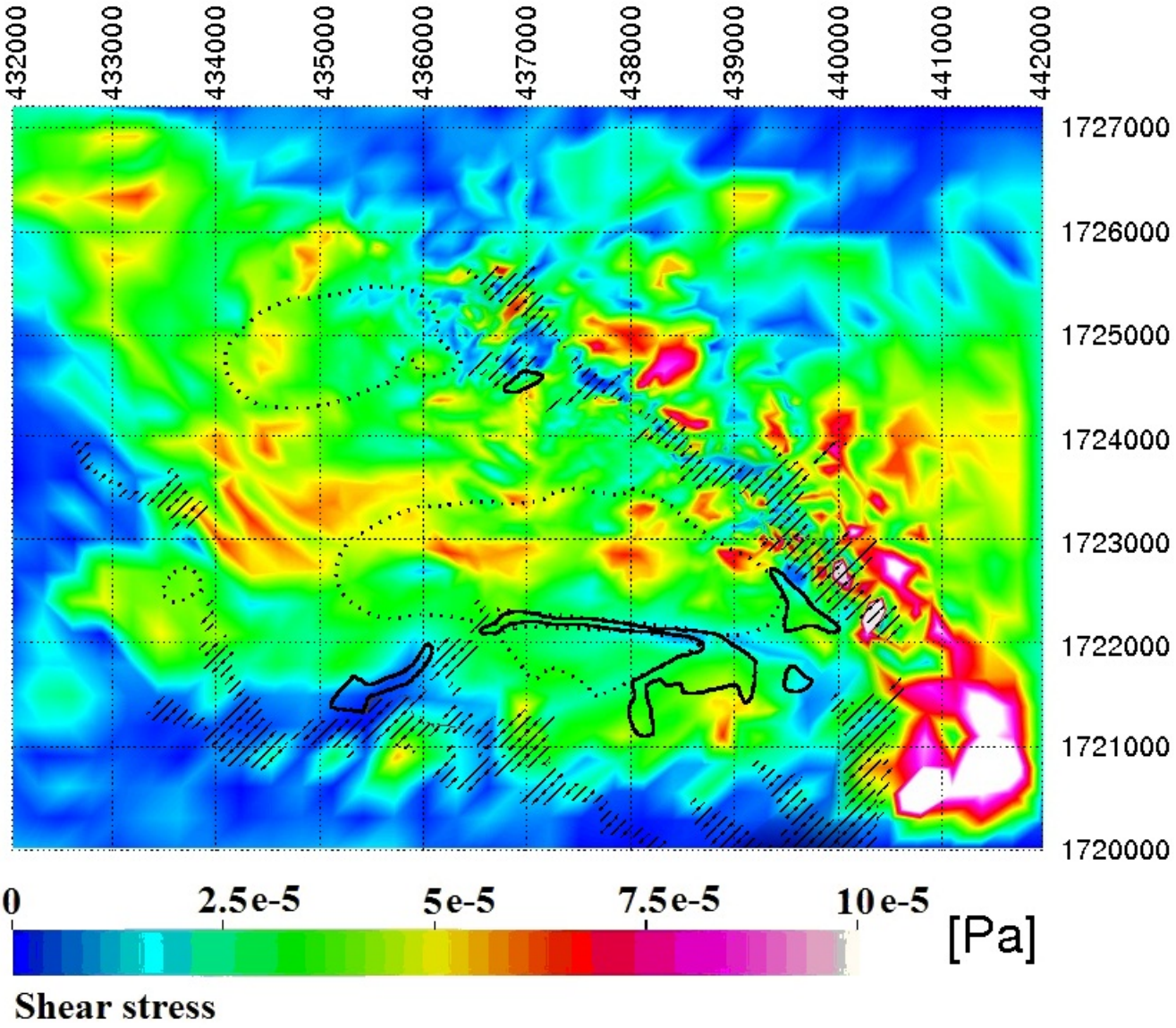

Figure 32: Results of the restart simulation with the katabatic profile acting as an inflow profile. This Figure indicates the absolute shear stress at 1000 seconds from initialization.

8 Conclusions

The simulations done in this work easily led to instabilities and convergence problems with the boundary conditions we used. Ideally, they would be embedded in regional climate models (RCM) or weather models that provide transient boundary conditions.

The compressibility should not be necessary to include in the equations since we are only interested in solving the flow of the SBB area, neither should the incompressibility assumption be false from a gas-dynamical point of view (low enough Mach-numbers) and from the temperature induced density difference (Raleygh numbers). In our point of view, as the katabatic winds build up further up the slope of the ice sheet, a Boussinesq approximation is not even needed, as the inertia of the arriving katabatic wind is so big that it is the dominating effect on the flow inside the valley.

Our results of the simulations with the ERA-interim re-analysis data acting as the inflow profiles do not confirm that the BIAs are formed solely due to average windspeeds and directions, as these winds do not cause very high velocities at these areas, see Figure 18. The accumulation of snow in the area where snow is observed to be accumulated (in the lee of the valley surrounding mountains) is partly explained by our results, since there are clear re-circulations in these areas. However our results do not provide strong enough evidence to verify the accumulation in these areas. These simulations can not be considered very reliable because of the channeled boundary conditions creating nozzles which lead to high velocity zones at some areas.

The katabatic wind simulation, with the inflow coming from the east, clearly indicates that there is an increase in velocity exactly at the BIAs. These winds as such could probably cause high enough speeds in this area to completely clear the BIA's, where parts of the old ice is believed to be ripped away from time to time, forming a clear surface in these areas. However, the open question is still if the high surface velocities are caused strictly by local pressure distributions causing katabatic winds, or is the reason for the extremely powerful winds a larger pressure area causing storms and katabatic winds to combine in these areas. We also need to point out that this simulation was strictly based on an assumed profile and wind direction, and this as such is not enough to be considered as an exact simulation of the reality, but it can definitely be considered as a valuable indicator that the local terrain actually causes the velocity gradients to increase at the exact positions where the BIAs are located.

We suggest that these BIA's might be cleared either by solely local katabatic winds

or due to extremely powerful temporal storms combined with katabatic winds that occur from time to time and cause wind speeds which would then lead to exaggerated shear stresses on the surface of the BIA's. Powerful surface forces would not only have effects on snow redistribution but they might also cause the surface ice to be ripped off. To verify this assumption, further research is necessary.

REFERENCES

Antarctic Connection. 2011. *Antarctic Connection.* Internet. http://www.antarcticconnection.com, checked April 28th, 2011.

Batchelor G. K. 2000. *An Introduction to Fluid Dynamics.* Cambridge University Press.

Bazilevs Y., Calo V. M., Cottrell J. A., Hughes T. J. R., Reali A., & Scovazzi G. 2007. Variational Multiscale Residual-Based Turbulence Modeling for Large Eddy Simulation of Incompressible Flows. *Comput. Methods Appl. Mech. Engrg.*, **197**(1-4), 173–201.

Bazilevs Y., Michler C., Calo V.M., & Hughes T.J.R. 2008. *Turbulence without Tears: Residual-Based VMS, Weak Boundary Conditions, and Isogeometric Analysis of Wall-Bounded Flows.* Tech. rept. Institute for Computational Engineering and Sciences, The University of Texas at Austin, 201 East 24th Street, 1 University Station C0200, Austin, TX 78712, USA.

Berrisford P., Dee D., Fielding K., Fuentes M., Kallberg P., Kobayashi S., & Uppala S. 2009 (August). *The ERA-Interim archive.* Tech. rept. 1. ECMWF, Shinfield Park, Reading.

Bintanja R. 1999. On the Glaciological, Meteorological, and Climatological Significance of Antarctic Blue Ice Areas. *Rev. Geophys.*, 337–359.

Gillet-Chaulet F., Gagliardini O., Meyssonnier J., Zwinger T., & Ruokolainen J. 2006. Flow-Induced Anisotropy in Polar Ice and Related Ice-Sheet Flow Modeling. *J. Non-Newtonian Fluid Mech.*, 33–43.

Gravemeier V. 2003. *The Variational Multiscale Method for Laminar and Turbulent Incompressible Flow.* Phd Thesis, Institut für Baustatik der Universität Stuttgart.

Gravemeier V., Lenz S., & Wall W.A. 2006. *Variational Multiscale Methods for Incompressible Flows.* Tech. rept. University of Göttingen, Technische Universität München, Germany, Boltzmannstr. 15, D-85747 Garching b. München.

Greve R., & Blatter H. 2009. *Dynamics of Ice Sheets and Glaciers.* 1st edn. Springer.

Grinsted A. 2006. *Advanced Methods of Glaciological Modeling and Time Series Analysis.* Phd Thesis, University of Oulu.

Hoffman J., & Johnson C. 2006. A New Approach to Computational Turbulence Modeling. *Comput. Methods Appl. Mech. Engrg.*, **195**(23-24), 2865–2880.

Hoffman J., & Johnson C. 2007. *Computational Turbulent Incompressible Flow.* Applied Mathematics: Body and Soul, vol. 4. Berlin: Springer.

Hughes T. J. R. 1995. Multiscale Phenomena: Green's Functions, the Dirichlet-to-Neumann Formulation, Subgrid Scale Models, Bubbles and the Origins of Stabilized Methods. *Computer Methods in Applied Mechanics and Engineering*, **127**(1-4), 387 – 401.

John V., Kindl A., & Suciu C. 2010. Finite Element LES and VMS Methods on Tetrahedral Meshes. *J. Comput. Appl. Math.*, **233**(April), 3095–3102.

Layton W. J. 2008. *Introduction to the Numerical Analysis of Incompressible Viscous Flows.* 1st edn. Society for Industrial and Applied Mathematic.

Luijting H. 2009. *Numerical Simulations of Katabatic Flow in Coats Land, Antarctica.* Phd Thesis, School of Environmental Sciences of the University of East Anglia.

Parish T. R., & Cassano J. J. 2003. Diagnosis of the Katabatic Wind Influence on the Wintertime Antarctic Surface Wind Field from Numerical Simulations. *Mon. Wea. Rev.*, **131**(June), 1128–1139.

Rautaheimo P. 2001. *Developments in Turbulent Modelling with Reynolds-Averaged Navier-Stokes Equations.* Phd Thesis, Helsinki University of Technology, Department of Mechanical Engineering.

Rodi W. 1984. *Turbulence Models and their Application in Hydraulics - a State of The-Art Review.* 2nd edn. University of Karlsruhe.

Sinisalo A. 2007. *Geophysical Exploration of Antarctic Blue Ice Areas (BIAs) for Paleoclimate Applications.* Phd Thesis, University of Oulu.

Sinisalo A., Grinsted A., & Moore J. C. 2004. Scharffenbergbotnen (Dronning Maud Land, Antarctica) Blue-Ice Area Dynamics. *Annals of Glaciology*, 417–422.

van As D., & van den Broeke M. R. 2006. Structure and Dynamics of the Summertime Atmospheric Boundary Layer over the Antarctic Plateau: 2. Heat, Moisture, and Momentum Budgets. *Journal of Geophysical Research*.

Zammett R. J., & Fowler A. C. 2006. *Katabatic Winds on Ice Sheets: A Refinement of the Prandtl Model*. Tech. rept. Mathematical Institute, Oxford University, Oxford, United Kingdom.

Zwinger T., & Moore J. C. 2009. Diagnostic and Prognostic Simulations with a Full Stokes Model Accounting for Superimposed Ice of Midtre Lovénbreen, Svalbard. *The Cryosphere*, 217–229.

Appendix A

Parts of the mesh extrusion code

```
// Compute layer thickness dZ for linear refinement:
//-----------------------------------------------------
double linearThickness(double S, double B, int levels)
{
  double dZ = 0.0;
  dZ = (S - B)/((double) levels - 1);
  return dZ;
}
// Compute layer cordinate Z for geometric refinement:
//-----------------------------------------------------
double refinedHeight(double S, double B, int levels, int level)
{
  double r = 1.2;
  int n = levels-2;
  double H = S-B;
  double a = H*(1-r)/(1-pow(r, n+1));
  double z = B;
  int k = 0;
  for(k = 0; k < level; ++k) {
    z = z + a * pow(r, k);
  }
  return z;
}
```

```
// Compute layer cordinate Z for geometric refinement at BL and uniform:
//-----------------------------------------------------
double refinedHeightBL (double S, double B, int levels,
  int level, int GL, double p, double r)
{

  int n = GL -1;
  double BL = (S - B)*p;
  double H = S-B;
  double a = BL *(1-r)/(1-pow(r, n+1));
  double z = B;
  double dZ = (S - B - BL)/((double) levels - GL -1);
  int k = 0;

  for(k = 0; k < level; ++k) {
    if(k<GL)
       z = z + a * pow(r, k);
    else
       z = z +  dZ;
  }
 return z;
}

  // write extruded mesh
  //--------------------
  for (j=0,level=0;level<levels;++level){
    for (k=0;k<nodesinpartition;++k){
      l=100*k/pointsinlevel;
      if (l>j){
j=l;
//printf("done: %3i percent\n", j);
      }

      // Geometrisesti tihennetty case:
      //-------------------------------

      double Z = refinedHeightBL(S[k], B[k],
```

```
      levels, level, GL, percentage, ratio);
    fprintf(outfids[1],"%i -1 %e %e %e\n",
      pointsinlevel*level + nodeinfo[k], X[k], Y[k], Z ); //
  }
}
```

Appendix B

Figures of the fitted polynomials

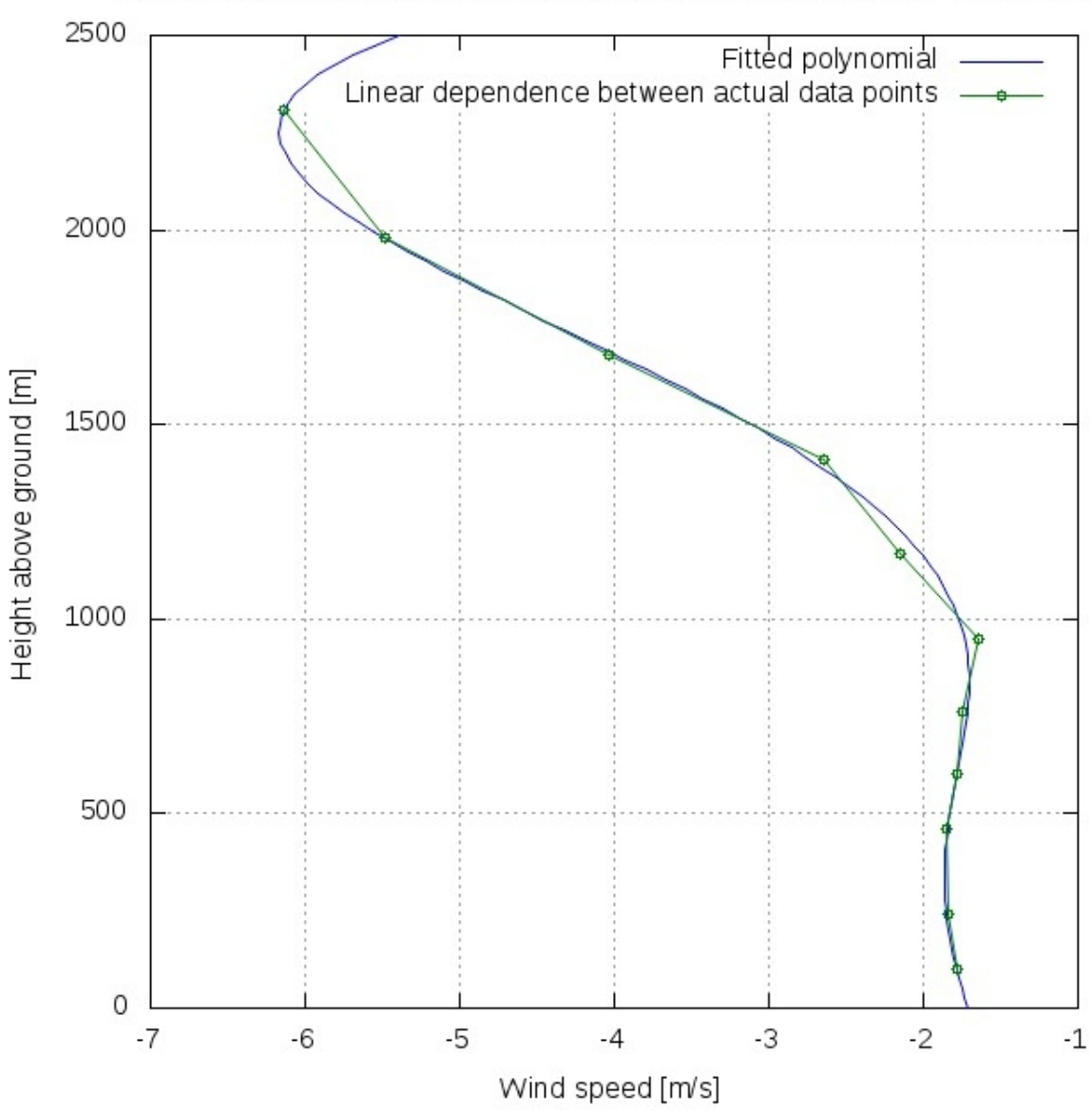

Figure B.1: Polynomial of the north components of the wind with mean velocity and direction

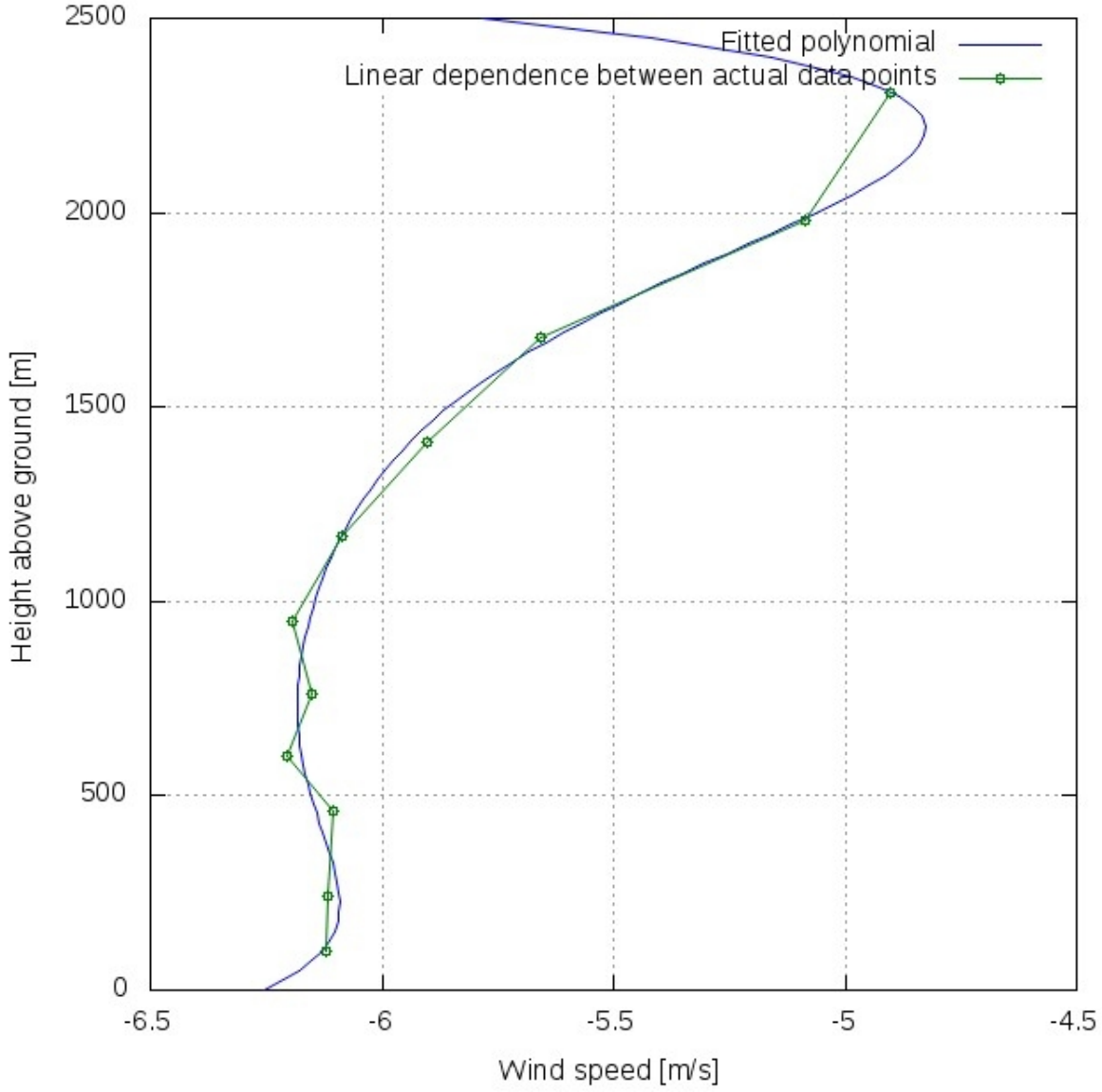

Figure B.2: Polynomial of the east components of the wind with mean velocity and direction

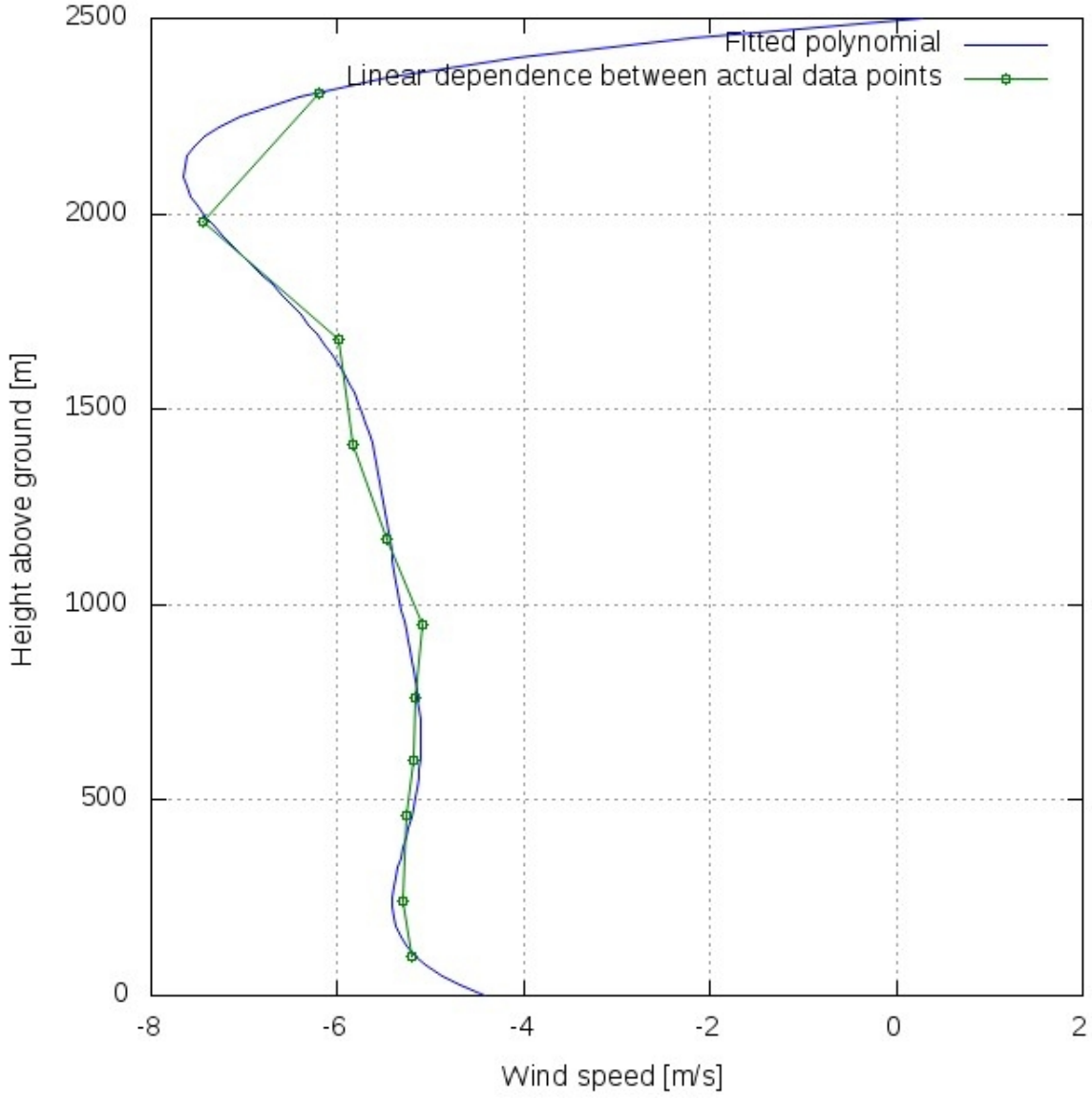

Figure B.3: Polynomial of the north components of the (more northerly) wind with a direction of the mean wind direction minus the deviation of the direction.

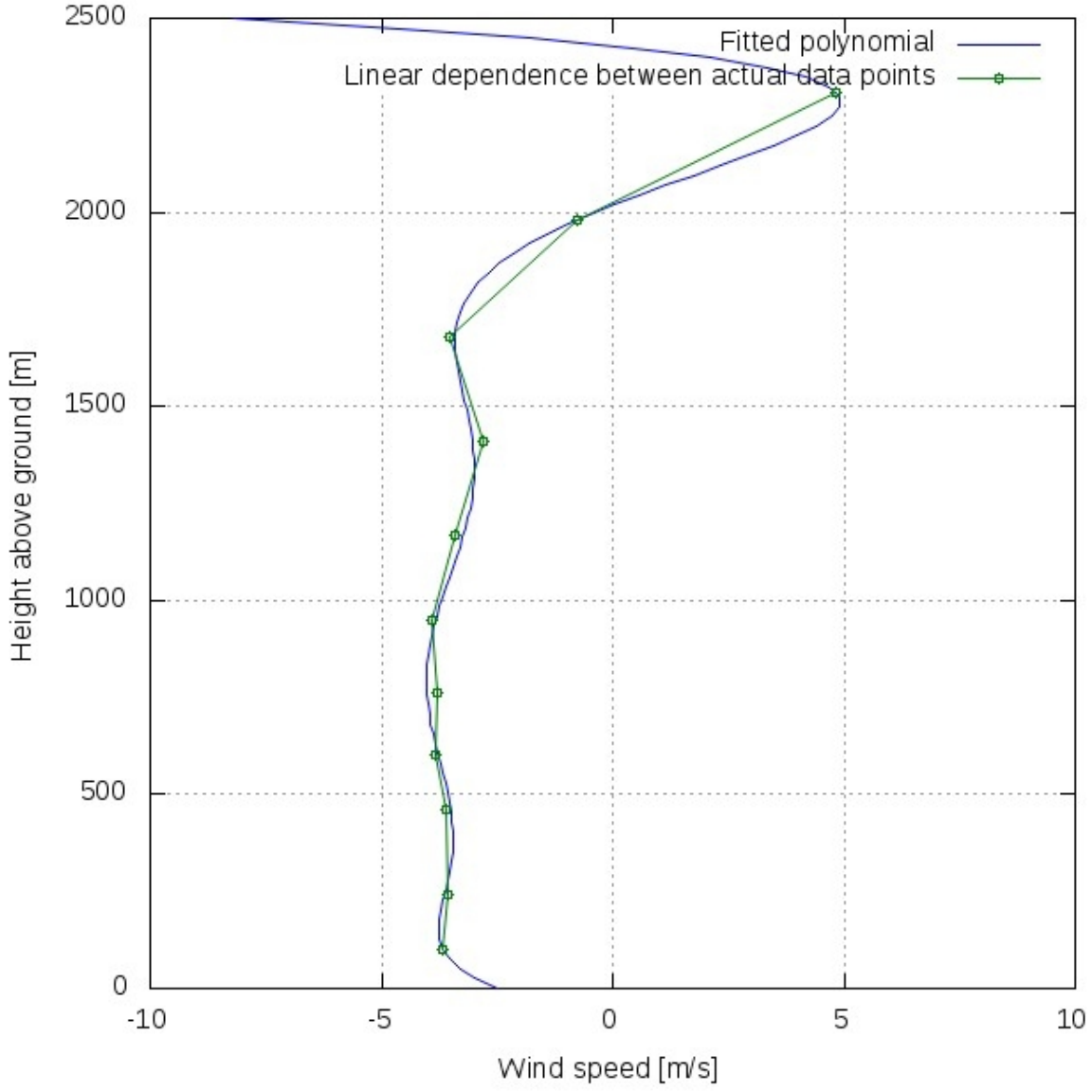

Figure B.4: Polynomial of the east components of the (more northerly) wind with a direction of the mean wind direction minus the deviation of the direction.

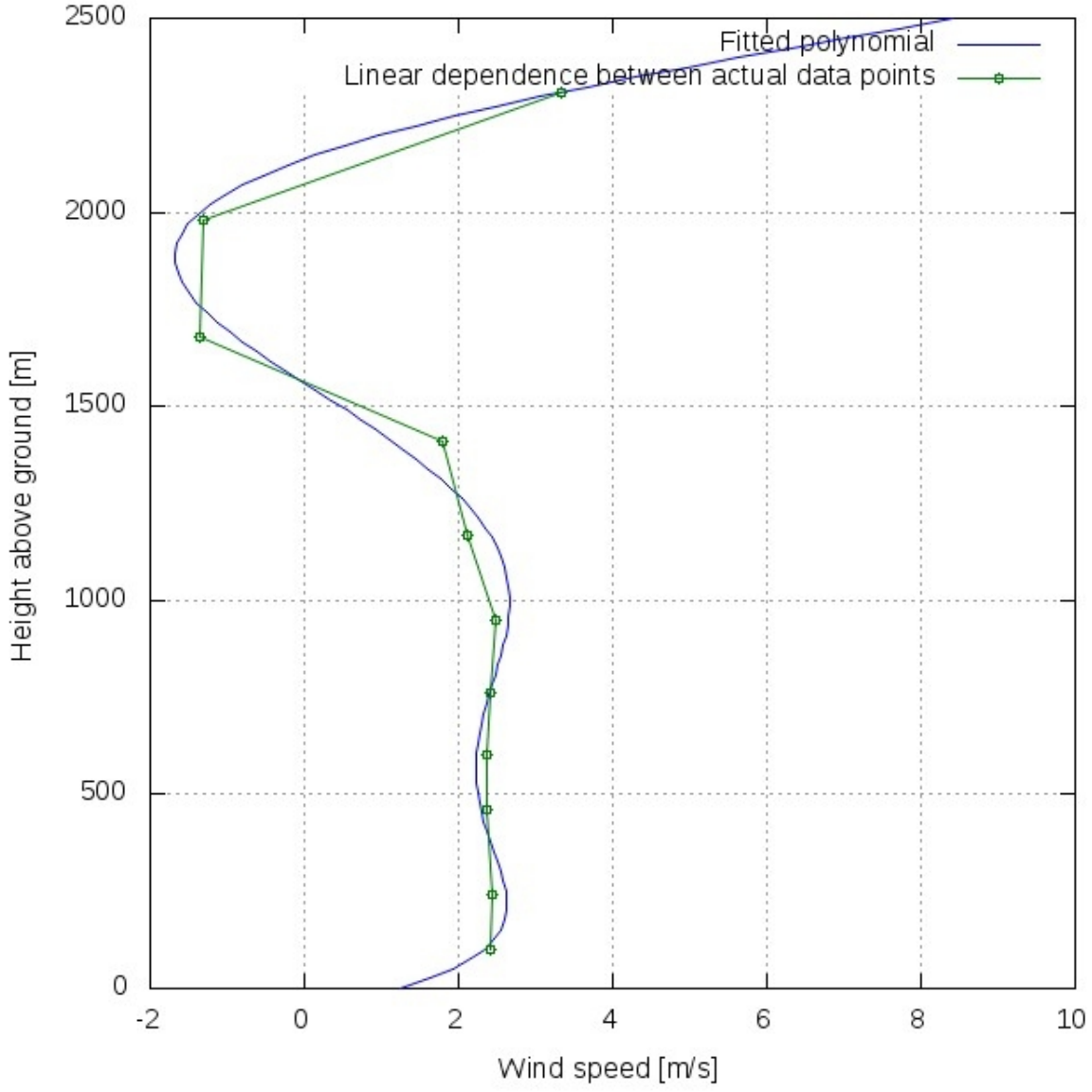

Figure B.5: Polynomial of the north components of the (more easterly) wind with a direction of the mean wind direction plus the deviation of the direction.

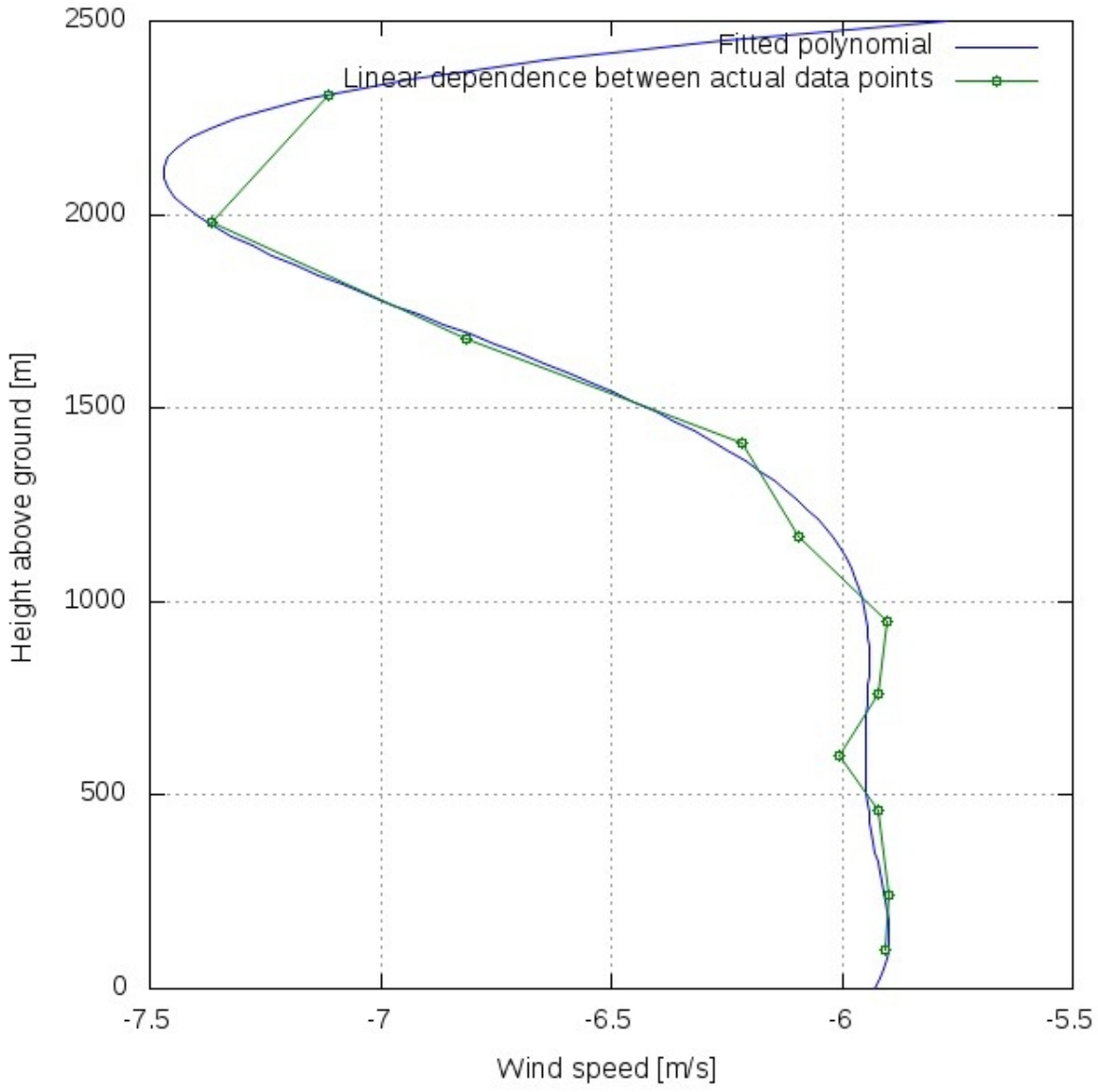

Figure B.6: Polynomial of the east components of the (more easterly) wind with a direction of the mean wind direction plus the deviation of the direction.